



NIH Public Access

Author Manuscript

J Phys Chem A. Author manuscript; available in PMC 2013 April 15.

Published in final edited form as:

J Phys Chem A. 2011 November 10; 115(44): 12055–12069. doi:10.1021/jp204499x.

Theory of Non-rigid Rotational Motion Applied to NMR Relaxation in RNA

Prashant S. Emani*, **Gregory L. Olsen^{‡,✉}**, **Gabriele Varani^{§,‡}**, and **Gary P. Drobny^{‡,*,¶}**

[‡]Department of Chemistry, University of Washington, Box 351700, Seattle, USA 98195

^{*}Department of Physics, University of Washington, Box 351560, Seattle, USA 98195

[§]Department of Biochemistry, University of Washington, Box 357350, Seattle, USA 98195

Abstract

Solution NMR spectroscopy can elucidate many features of the structure and dynamics of macromolecules, yet relaxation measurements, the most common source of experimental information on dynamics, can only sample certain ranges of dynamic rates. A complete characterization of motion of a macromolecule therefore requires the introduction of complementary experimental approaches. Solid-state NMR successfully probes the nanoseconds to microseconds (ns to μ s) time scale, a dynamic window where solution NMR results have been deficient, and probes conditions where the averaging effects of rotational diffusion of the molecule are absent. Combining the results of the two distinct techniques in a single framework provides greater insight into dynamics, but this task requires the common interpretation of results recorded under very different experimental conditions. Here we provide a unified description of dynamics that is robust to the presence of large-scale conformational exchange, where the diffusion tensor of the molecule varies on a time scale comparable to rotational diffusion in solution. We apply this methodology to the HIV-1 TAR RNA molecule, where conformational rearrangements are both substantial and functionally important. The formalism described herein is of greater generality than earlier combined solid state/solution NMR interpretations, if detailed molecular structures are available, and can offer a more complete description of RNA dynamics than either solution or solid state NMR alone.

Keywords

HIV-1 TAR RNA; nucleic acids; conformational capture; relaxation times; rotational diffusion; combined solid-state and solution NMR

1. Introduction

The last few years have seen a growing interest in the roles played by motion and conformational adaptation in mediating protein-nucleic acid interactions. It is now widely recognized that many RNAs^{1–13} and some DNAs^{14–17} function by undergoing large conformational changes when binding to proteins or small molecule ligands. In some cases, fluctuations of the native structure may pre-dispose an RNA or DNA sequence to form interactions with other molecules, suggesting that a protein may in effect “capture” a structurally labile nucleic acid as it fluctuates through a conformation that is optimized for binding. Therefore a thorough description of the physical basis for specific recognition

[¶]Address correspondence to: Gary Drobny, drobny@chem.washington.edu, 1-206 685 8665 (Fax).

[✉]Current address: Department of Chemical Physics, Weizmann Institute of Science, PO Box 26, Rehovot 76100, Israel.

requires that static structural data obtained by crystallography and/or NMR are augmented by information on the conformational changes that each component undergoes to form a complex. Such information includes the dynamic amplitudes associated with functionally relevant structural changes and the rates at which such structural changes occur.

A classical paradigm for the importance of dynamics in RNA function is provided by the transactivation response element (TAR) RNA (Figure 1) from the human immunodeficiency virus type-1 (HIV-1). This RNA plays a role in transcription elongation and is thus required for HIV replication, making it a potential drug target. Relevant to the present investigation, binding of TAR RNA to the HIV-1 Tat protein requires extensive structural rearrangement of the RNA.^{1–9} The structural properties of the bound and unbound conformational states of TAR RNA are known,^{5,18–20} yet, despite recent progress,^{21,22} there is still considerable uncertainty regarding how these structural changes occur. For example, it is not yet certain whether the TAR RNA is driven into its bound structural state only upon actual contact with Tat, or if TAR fluctuates through a structural state optimized for binding that is subsequently “captured” by the Tat protein, or some combination of the two mechanisms.

The local dynamics of TAR RNA have been analyzed using a variety of NMR approaches, including solution NMR relaxation methods.^{7,21,23} Detailed studies of ¹³C/¹H line widths and relaxation rates in and around the bulged loop of native TAR, and the measurement of residual dipolar couplings (RDCs), have provided strong evidence for the existence of ns- μ s time scale collective motions of the distal helices about a dynamic hinge associated with the bulged loop of TAR.^{21,24} TAR mutants consisting of elongated distal helices were used to demonstrate that these concerted helical motions occur at rates nearly coincident with the time scale of the overall tumbling in native TAR.^{21,25} The proposed helical motions are significant enough in amplitude to deform the tumbling TAR molecule and affect its hydrodynamics.²⁶

These solution NMR relaxation and RDC data have been interpreted as supporting a conformational capture mechanism as the basis for the TAR-Tat interaction, but quantitative interpretation of solution NMR data in terms of a specific sequence of structural changes of TAR has been elusive due in part to the complexity of the dynamic mode-coupling problem.^{21,25,27} In a recent paper, we considered the problem of the non-rigid tumbling of TAR, motivated by solid-state NMR (ssNMR) results²² suggesting that the rate of hydrodynamically-significant helical domain motions occur on a timescale significantly longer than the characteristic molecular tumbling times. By extrapolating to the case of infinitely slow exchange between discrete TAR conformers in solution, we simplified the problem to two independently tumbling molecular conformers, each of which contributed to a fraction of the solution T₁ and T₂ relaxation rates determined by its probability of occurrence. This *slow-exchange* (SE) formalism was applied to the dynamics observed for residue U-38, a base paired residue in TAR RNA, for which the rate and amplitude of conformational exchange were obtained using ²H ssNMR by incorporating uridine-5,6-²H₂ at the U38 residue.^{22,28} Not only did the SE formalism account for the relaxation properties of the ¹³C spins of U-38, but with small adjustments to account for minor structural variations, the solution relaxation properties of all pyrimidine ¹³C spins in the upper helix of TAR could be accounted for as well.

In the current manuscript, we develop a theory of non-rigid biomolecular rotation that allows for an arbitrary rate of exchange between conformers, in effect relaxing the SE assumption of our previous work. We apply the expressions for the solution T₁ and T₂ relaxation rates derived herein to the motion of C6-H6 bond of the U38 residue. While comparisons to solution data in this manuscript are limited to relaxation times for the U38-¹³C site, the method is applicable to any site and residue for which motional models

(ssNMR-derived or otherwise) are available. Expressions are obtained for the case of instantaneous jumps between discrete conformers with arbitrary rotational diffusion tensors, and solution relaxation rates are calculated for various motional parameters.

In section 2, we present the derivation of the expressions for the solution T_1 and T_2 relaxation times for a general rate of exchange between conformers. We also reiterate the solid-state models used in the simulations. In section 3, we present the results obtained when applying our theory to sets of structures generated by the artificial modification of upper helical angles relative to the lower helix, after showing the correspondence of results of the general theory with those of the slow exchange formalism from the previous approach. In section 4, we discuss these results and their implications for understanding the full range of dynamics of TAR-RNA under two different sets of sample conditions.

2. Theory

In this section, we derive an expression for the correlation function for a reorienting macromolecule, modeled as a Brownian rotator, and characterized by a fully anisotropic diffusion tensor. As a result of conformational changes occurring within the RNA, the molecular shape changes in such a way as to make the diffusion tensor time-dependent. This time dependence of the diffusion tensor is modeled as an exchange between discrete structural conformers, as described in our prior work.²² However, in the present work, the assumption of time scale separation between the rate of conformational exchange and molecular reorientation is not made. The two types of motion may therefore occur at arbitrary time scales.

Rotational diffusion for a fully-anisotropic diffusion tensor has been previously considered in a number of cases. Perrin derived the time correlation function for rotational diffusion about three perpendicular axes of an ellipsoid and used the expression to calculate the fluorescence depolarization that results from the rotation of ellipsoidal molecules in solution.²⁹ Woessner³⁰ extended Perrin's formalism to calculate spectral densities and then the rate of Zeeman relaxation of dipole-coupled spins attached to a reorienting ellipsoid. Favro³¹ exploited the similarity of the rotational diffusion equation to Schrödinger's equation for a rigid rotor. For a rigid body with an axis of symmetry, Favro showed that the Green's function (i.e. conditional probability) is a linear combination of rigid rotor eigenfunctions. For a fully asymmetric diffusion tensor, this expansion is only approximate, but the first few eigenfunctions and their coefficients were calculated. Huntress extended the isotropic diffusion equation to account for fully anisotropic rotation and solved for the relaxation time of a nuclear spin undergoing fully anisotropic rotational diffusion assuming a number of spin interaction mechanisms.³² Huntress also showed how the measurement of the relaxation times of appropriate nuclei in the molecule can give the full rotational diffusion tensor. A similar approach was used by Freed to calculate the rate of electron spin relaxation resulting from anisotropic rotational diffusion.³³

These approaches all aimed to solve the diffusion equation for fully anisotropic rotational diffusion tensors, but differed in the specific mathematical techniques used to reach this end. For example, Woessner used the direction cosine formalism to construct a correlation function for rotation of ellipsoidal molecules, whereas Favro formulated basically the same problem using Cayley-Klein coordinates. We have repeated the analysis as follows, and explicitly present the derivation in a slightly different manner for clarity.

The evaluation of relaxation times in solid-state and solution NMR requires the evaluation of ensemble-averaged two-time correlations functions of the orientations of the labeled site. The orientation function often takes the form of a Legendre polynomial whose argument is the dot product between the unit vectors $\hat{n}(\tau)$ at time $\tau = 0$ and time $\tau = t$. This is the case for

a molecule that is freely diffusing in a solvent. The expression for this polynomial can be expanded using the well-known addition theorem for spherical harmonics (see, for example, Jackson³⁴):

$$\left\langle P_l(\hat{n}(0).\hat{n}(t)) \right\rangle = \frac{4\pi}{2l+1} \sum_{m=-l}^l \left\langle Y_{lm}(\hat{n}(0)) Y_{lm}^*(\hat{n}(t)) \right\rangle \quad (1)$$

The unit vector orientations of the labeled site in the above equation are given in the laboratory frame of the experiment. In order to simplify the evaluation of the given expression we can define a molecule-fixed frame that rotates relative to the lab frame and express the orientation functions in terms of the vector position of the labeled site in this molecule-fixed frame. This is achieved by expressing the spherical harmonics of the laboratory frame orientations as rotated functions of spherical harmonics in the molecule-fixed frame. Moreover, since the motion considered here is the free-diffusion of the tumbling molecule in the solvent, it is reasonable to use the diffusion tensor principal axis frame (PASd) as the molecule-fixed frame.

$$\left\langle P_l(\hat{n}(0).\hat{n}(t)) \right\rangle = \frac{4\pi}{2l+1} \sum_{m=-l}^l \left\langle Y_{lm}(\hat{n}(0)) Y_{lm}^*(\hat{n}(t)) \right\rangle = \frac{4\pi}{2l+1} \sum_{m=-l}^l \left(\sum_{a,a'=-l}^l \left\langle D_{ma}^{(l)*}(\vec{\Omega}_0) Y_{la'}(\theta_0, \phi_0) D_{ma}^{(l)}(\vec{\Omega}_t) Y_{la}^*(\theta_t, \phi_t) \right\rangle \right) \quad (2)$$

Here, $\vec{\Omega}_0$ and $\vec{\Omega}_t$ are the Euler angle rotations required to rotate the PASd frame into the laboratory frame, the (θ, ϕ) angles are the orientations of the labeled site vectors in the PASd frame, the $D_{mn}^{(l)}$'s are the Wigner rotation matrices of angular momentum l following the convention of Rose³⁵ and Tinkham³⁶:

$$D_{mn}^{(l)}(\alpha, \beta, \gamma) = e^{-im\alpha} d_{mn}^{(l)}(\beta) e^{-in\gamma} \quad (3)$$

In this work, we want to consider the effect of including exchanges between conformers with different diffusion tensors. The effect of such exchange on the correlation function is calculated below by generalizing the method of Wong, Case and Szabo³⁷ to include diffusion tensors with three distinct eigenvalues (i.e. a fully-anisotropic tensor). As a first step, we can explicitly separate out the dependence of the ensemble average on the relative populations of the various conformers, with the conformer at time $\tau = 0$ being labeled as α , and the conformer at time $\tau = t$ being labeled as β :

$$\left\langle P_l(\hat{n}(0).\hat{n}(t)) \right\rangle = \frac{4\pi}{2l+1} \sum_{m,a,a'=-l}^l \sum_{\alpha,\beta=1}^{N_{Conformers}} \left\langle D_{ma}^{(l)*}(\vec{\Omega}_0) D_{ma}^{(l)}(\vec{\Omega}_t) \right\rangle_{\alpha\beta} Y_{la'}(\theta_\alpha, \phi_\alpha) Y_{la}^*(\theta_\beta, \phi_\beta) P_{eq}(\alpha) \quad (4)$$

Here $P_{eq}(\alpha)$ is the *a priori* the probability of finding the molecule in conformation α .

In this formalism, the problem is reduced to an evaluation of $\left\langle D_{ma}^{(l)*}(\vec{\Omega}_0) D_{ma}^{(l)}(\vec{\Omega}_t) \right\rangle_{\alpha\beta}$ for tumbling motion that occurs while the molecule also exchanges between various conformers with different diffusion tensors. First, we will find the probability for a *single conformer* to transition from an orientation of Ω_0 at time $\tau = 0$ to an orientation of Ω_t at time $\tau = t$; the results of this calculation will then be generalized to incorporate exchange between different conformers. Considering that problems of interest in solid-state and solution NMR mostly, if not always, involve tensors of order $I = 2$, we will confine attention in the following to the evaluation of correlation functions of $I = 2$ rotation matrices.

A. General solution to single conformer diffusion equation

The free-diffusion equation for a rigid-body rotor is:

$$\frac{\partial}{\partial t} P(\vec{\Omega}, t) = - \sum_{i,j=1}^3 \hat{L}_i D_{ij} \hat{L}_j P(\vec{\Omega}, t) \quad (5)$$

Here the operators \hat{L}_i represent the angular momentum operator about the i^{th} axis and $P(\vec{\Omega}, t)$ is the probability that the molecular axis system will have rotated through an Euler angle vector $\vec{\Omega}$ at a time t relative to its initial orientation in the laboratory frame at time $t=0$. The coefficients D_{ij} are the elements of the 2nd order rotational diffusion tensor for the molecule.

The right hand side (RHS) of the equation can be expanded in the principal axis frame of the diffusion tensor (PASd), where the diffusion tensor is diagonal and has eigenvalues $\{D_x, D_y, D_z\}$:

$$\sum_{i,j=1}^3 \hat{L}_i D_{ij} \hat{L}_j = D_x \hat{L}_x^2 + D_y \hat{L}_y^2 + D_z \hat{L}_z^2 \quad (6)$$

This expression can be further rewritten in terms of the operators \hat{L}_z^2 , \hat{L}_z and $\hat{L}_{\pm} = \hat{L}_x \pm i\hat{L}_y$, the lowering/raising (+/-) operators for the z-angular momentum (the \hat{L}_{+} operator is the lowering operator when the operators are expressed in the PASd frame as opposed to the laboratory frame; this occurs because the commutation relations between operators change sign in transforming from the laboratory to the PASd frame):

$$\sum_{i,j=1}^3 \hat{L}_i D_{ij} \hat{L}_j = D_x \hat{L}_x^2 + D_y \hat{L}_y^2 + D_z \hat{L}_z^2 = D_z \hat{L}_z^2 + D_{\perp} \left(\hat{L}_{\perp}^2 - \hat{L}_z^2 \right) + \frac{\Delta}{4} (\hat{L}_{+}^2 + \hat{L}_{-}^2) \quad (7)$$

In Eq 7, $D_{\perp} = \frac{D_x + D_y}{2}$ and $\Delta = D_x - D_y$. The assumption in this formalism is that the component D_z is the largest eigenvalue of the diffusion tensor, followed by D_x and finally D_y . It is easy to redefine the axes to suit any of the situations ranging from a prolate ellipsoid to an oblate ellipsoid and for all the fully-anisotropic cases in between these two extremes.

The problem simplifies considerably in the cylindrically-symmetric case of $D_x = D_y$. The eigenfunctions of the diffusion operator in this instance are eigenfunctions of the operators \hat{L}_z^2 and \hat{L}_z , and can be expressed in terms of the Wigner rotation matrices:

$$|l, m, k\rangle = \left(\frac{2l+1}{8\pi^2} \right)^{1/2} D_{mk}^{(l)*}(\alpha, \beta, \gamma) \quad (8)$$

where $\{\alpha, \beta, \gamma\}$ are the Euler angles that transform from the PASd frame to the laboratory frame.

In order to proceed to the fully-anisotropic case, it is useful to understand the Wigner

rotation matrices from a geometric perspective: as $D_{mk}^{(l)}(\vec{\Omega} = \{\alpha, \beta, \gamma\}) = \langle l, m | e^{-i\vec{L} \cdot \vec{\Omega}} | l, k \rangle$, the

Wigner rotation matrices may be considered as the overlap between the eigenkets of the $\widehat{\vec{L}}^2$ operator expressed in the laboratory ($\{\hat{L}_X, \hat{L}_Y, \hat{L}_Z\}$) and diffusion frames ($\{\hat{L}_X, \hat{L}_Y, \hat{L}_Z\}$), where the two frames are connected by an Euler transformation denoted as $\Omega = \{\alpha, \beta, \gamma\}$. In the expression $e^{-i\vec{L}\cdot\vec{\Omega}}$, it is understood that the angular momentum operator is expanded in an Euler angle basis, to match the symbolic representation of $\Omega = \{\alpha, \beta, \gamma\}$. The angular momentum operators in one of the frames commute with all the operators in the other frame. Thus, given that the rotational diffusion operator, as expressed in Eq 6, commutes with both $\widehat{\vec{L}}^2$ and with ($\{\hat{L}_X, \hat{L}_Y, \hat{L}_Z\}$), the eigenvalues l and m from Eq 8, where m is associated with the laboratory frame operator \hat{L}_Z , will be good eigenvalues even for the fully-anisotropic diffusion equation.

Therefore, we can conclude that the general solution to the fully-anisotropic problem can be expressed as a linear combination of the Wigner rotation matrices:

$$P(\vec{\Omega}, t \mid \vec{\Omega}_0) = \sum_{l=0}^{\infty} \sum_{m=-l}^l \left(\sum_{p_l=1}^{2l+1} \left(\sum_{k=-l}^l F_{lk}^{(p_l)}(\vec{\Omega}_0, t) D_{mk}^{(l)*}(\vec{\Omega}) \right) \right) \quad (9)$$

where the index p_l represents the label of the eigenvalue of the diffusion operator for a fixed value of the angular momentum l , and runs from 1 to 5 in the present work. In order to show how this expansion may be achieved, we next consider the operator expressed for a value of $l=2$, since this is the case relevant to solid state NMR applications.

Using the notation $\widehat{H} = D_z \widehat{L}_z^2 + D_{\perp} \left(\widehat{\vec{L}}^2 - \widehat{L}_z^2 \right) + \frac{\Delta}{4} (\widehat{L}_+^2 + \widehat{L}_-^2)$, we can define the matrix $H_{k'k}^{(l)} = \langle l, m, k' \mid \widehat{H} \mid l, m, k \rangle$ and express it for the case of $l=2$ as:

$$\widehat{H}^{(2)} = \begin{pmatrix} 4D_z + 2D_{\perp} & 0 & \frac{\Delta\sqrt{6}}{2} & 0 & 0 \\ 0 & D_z + 5D_{\perp} & 0 & \frac{3\Delta}{2} & 0 \\ \frac{\Delta\sqrt{6}}{2} & 0 & 6D_{\perp} & 0 & \frac{\Delta\sqrt{6}}{2} \\ 0 & \frac{3\Delta}{2} & 0 & D_z + 5D_{\perp} & 0 \\ 0 & 0 & \frac{\Delta\sqrt{6}}{2} & 0 & 4D_z + 2D_{\perp} \end{pmatrix} \quad (10)$$

The rows and columns are labeled from right to left and top to bottom by $k = -2, -1, 0, 1, 2$. The off-diagonal elements have been computed using the properties of the lowering and raising operators $\hat{L}_{\pm} = \hat{L}_x \pm i\hat{L}_y$:

$$\langle l, m, k \mid \widehat{L}_+^2 + \widehat{L}_-^2 \mid l, m, k \pm 2 \rangle = \sqrt{l(l+1) - (k \pm 2)(k \pm 1)}. \sqrt{l(l+1) - (k \pm 1)k} \quad (11)$$

The eigenvalues and eigenvectors of the above operator matrix will be linear combinations of the Wigner rotation matrices of order $l=2$. Moreover, as the matrix is real and symmetric, and given that the Wigner rotation matrices are orthogonal with respect to the indices l , m and k , the matrix $\widehat{H}^{(2)}$ will yield eigenvectors that are orthogonal for non-degenerate eigenvalues.

The eigenvalues and eigenvectors of the matrix $\overleftrightarrow{H}^{(2)}$ are listed in Table 1, where the eigenvector elements are listed as the coefficients of the 2nd order Wigner rotation matrix $D_{mk}^{(l)}(\vec{\Omega})$ for $k = -2, -1, 0, 1, 2$. The quantity Σ is defined as:

$$\Sigma = (D_x^2 + D_y^2 + D_z^2) - (D_x D_y + D_y D_z + D_z D_x).$$

The same procedure may be in principle repeated for all values of $l = 1, \dots, \infty$. However, due to the orthogonality of the Wigner matrices, the correlation functions of Wigner matrices of order l may be also calculated exactly with an evaluation of the eigenvalues and eigenvectors of the matrix $\overleftrightarrow{H}^{(l)}$ alone. We define the functions

$$A_{mp_l}^{(l)*}(\vec{\Omega}) = \left(\frac{2l+1}{8\pi^2}\right)^{1/2} \sum_{k=-l}^l f_{l,k}^{(p_l)} D_{mk}^{(l)*}(\vec{\Omega}) \quad (12)$$

which satisfy the orthogonality relation

$$\begin{aligned} \int d\vec{\Omega} A_{mp_l}^{(l)*}(\vec{\Omega}) A_{m'p_l'}^{(l')}(\vec{\Omega}) &= \left(\frac{2l+1}{8\pi^2}\right)^{1/2} \left(\frac{2l'+1}{8\pi^2}\right)^{1/2} \sum_{k=-l}^l \sum_{k'=-l}^l f_{l,k}^{(p_l)} f_{l',k'}^{(p_l')} \int d\vec{\Omega} D_{mk}^{(l)*}(\vec{\Omega}) D_{m'k'}^{(l')}(\vec{\Omega}) \\ &= \sum_{k=-l}^l \sum_{k'=-l}^l f_{l,k}^{(p_l)} f_{l',k'}^{(p_l')} \delta_{ll'} \delta_{mm'} \delta_{kk'} \\ &= \delta_{ll'} \delta_{mm'} \sum_{k=-l}^l f_{l,k}^{(p_l)} f_{l,k}^{(p_l')} \end{aligned} \quad (13a)$$

where the orthogonality of the Wigner matrices was used

$$\int d\vec{\Omega} D_{mk}^{(l)*}(\vec{\Omega}) D_{m'k'}^{(l')}(\vec{\Omega}) = \frac{8\pi^2}{2l+1} \delta_{ll'} \delta_{mm'} \delta_{kk'} \quad (14)$$

Given that the eigenvectors whose elements are represented by the $f_{l,k}^{(p_l)}$'s are orthonormal, the summation in the second line of Equation 13a contracts to a Kronecker delta in the indices p_l and p_l' , yielding:

$$\int d\vec{\Omega} A_{mp_l}^{(l)*}(\vec{\Omega}) A_{m'p_l}^{(l)}(\vec{\Omega}) = \delta_{ll'} \delta_{mm'} \delta_{p_l p_l'} \quad (13b)$$

Using this relation, and the initial condition $P(\vec{\Omega}, 0 | \vec{\Omega}_0) = \delta(\vec{\Omega} - \vec{\Omega}_0)$, it can be shown that the transition probability takes the form

$$P(\vec{\Omega}, t | \vec{\Omega}_0) = \sum_{l=0}^{\infty} \sum_{m=-l}^l \sum_{p_l=1}^{2l+1} e^{-\lambda_{p_l}^{(l)} t} A_{mp_l}^{(l)}(\vec{\Omega}_0) A_{mp_l}^{(l)*}(\vec{\Omega}) \quad (15)$$

B. Solution of the conformational exchange problem

Having solved the problem of single diffusion for a molecule with a single conformer, we follow the approach of Wong, Case and Szabo³⁷ in formulating the problem of a molecule exchanging between different conformers with different diffusion tensors while also undergoing diffusive motion. The equation of rotational motion is a coupling of the free-diffusion operator for a single conformer with discrete, instantaneous jumps between different conformations:

$$\frac{\partial}{\partial t} P(\vec{\Omega}, \beta, t | \vec{\Omega}_0, \alpha) = - \sum_{i,j=1}^3 \widehat{L}_i D_{ij}^\beta \widehat{L}_j P(\vec{\Omega}, \beta, t | \vec{\Omega}_0, \alpha) + \sum_{\gamma=1}^{N_{Conformers}} R_{\beta\gamma} P(\vec{\Omega}, \gamma, t | \vec{\Omega}_0, \alpha) \quad (16)$$

Here $P(\vec{\Omega}, \beta, t | \vec{\Omega}_0, \alpha)$ is the transition probability from the previous section with the additional condition that the molecule starts in conformation α at time $\tau = 0$ and is in conformation β at time $\tau = t$.

The $R_{\beta\gamma}$'s are the weighted rates of transition from conformations γ to

β , =Jump rate $\times \sqrt{\frac{P_{eq}(\beta)}{P_{eq}(\gamma)}}$, where the weighted rate with $\beta = \gamma$ is the negative of the sum of the weighted rates of transition away from β into other conformations. The weighted rates are used instead of the bare jump rates (which are the numbers regularly quoted in this manuscript) in order to satisfy the condition of detailed balance. It is assumed that the transitions between conformations are instantaneous, and that the diffusion tensor principal axes of each conformer coincide with those of the previous conformer at the instant of transition. These assumptions can be mitigated to a certain extent by increasing the number of structural conformations in the trajectory of the molecule, thereby approximating the situation of continuous underlying atomic motion more closely.

Utilizing the Euler angle dependence from Eq 15, and generalizing the time dependence of the solution from simple eigenvalue evolution so as to accommodate conformational exchange, we obtain

$$P(\vec{\Omega}, \beta, t | \vec{\Omega}_0, \alpha) = \sum_{l=0}^{\infty} \sum_{m=-l}^l \left(\sum_{p_l=1}^{2l+1} c_{lp_l}^{\beta\alpha}(t) A_{mp_l}^{(l)}(\vec{\Omega}_0) A_{mp_l}^{(l)*}(\vec{\Omega}) \right) \quad (17)$$

Upon substituting Eq 17 into Eq 16 and using the orthogonality relation (Eq 13b) we arrive upon the set of equations that determine the time-dependent coefficients $c_{lp_l}^{\beta\alpha}(t)$:

$$\frac{dc_{lp_l}^{\beta\alpha}(t)}{dt} = -\lambda_{p_l}^{(l)} c_{lp_l}^{\beta\alpha}(t) + \sum_{\gamma=1}^{N_{Conformers}} R_{\beta\gamma} c_{lp_l}^{\gamma\alpha}(t) \quad (18)$$

The right hand side of Eq 18 can be written as a jump matrix between conformers and the eigenvalues and eigenvectors can be used to solve for the $c_{lp_l}^{\beta\alpha}(t)$'s.

C. Evaluation of the correlation functions between Wigner rotation matrices

Returning to the central problem of evaluating $\left\langle D_{ma}^{(l)*}(\vec{\Omega}_0) D_{ma}^{(l)}(\vec{\Omega}_t) \right\rangle_{\alpha\beta}$, we can use Eq 17 along with orthogonality relations between Wigner Matrices and a uniform *a priori*

probability of $P(\vec{\Omega}_0) = \frac{1}{8\pi^2}$ to obtain the final result:

$$\begin{aligned}
 & \left\langle D_{ma}^{(l)*}(\vec{\Omega}_0) D_{ma}^{(l)}(\vec{\Omega}_t) \right\rangle_{\alpha\beta} \\
 &= \int d\vec{\Omega}_0 \int d\vec{\Omega}_t P(\vec{\Omega}_0) P(\vec{\Omega}_t, \beta, t | \vec{\Omega}_0, \alpha) D_{ma}^{(l)*}(\vec{\Omega}_0) D_{ma}^{(l)}(\vec{\Omega}_t) \\
 &= \int d\vec{\Omega}_0 \int d\vec{\Omega}_t P(\vec{\Omega}_0) D_{ma}^{(l)*}(\vec{\Omega}_0) D_{ma}^{(l)}(\vec{\Omega}_t) \sum_{L=0}^{\infty} \sum_{M=-L}^L \sum_{p_l=1}^{2L+1} c_{lp_l}^{\beta\alpha}(t) A_{MP_L}^{(L)}(\vec{\Omega}_0) A_{MP_L}^{(L)*}(\vec{\Omega}_t) \\
 &= \sum_{L=0}^{\infty} \sum_{M=-L}^L \sum_{p_l=1}^{2L+1} c_{lp_l}^{\beta\alpha}(t) \left(\frac{1}{2L+1} \right) \sum_{K,K'=-L}^L f_{L,K}^{(P_L)} f_{L,K'}^{(P_L)} \delta_{Ll} \delta_{K'a} \delta_{Ka} \delta_{Mm} \\
 &= \left(\frac{1}{2l+1} \right) \sum_{p_l=1}^{2l+1} c_{lp_l}^{\beta\alpha}(t) f_{l,a}^{(p_l)} f_{l,a'}^{(p_l)}
 \end{aligned} \tag{19}$$

Using the final expression of Eq 19 in Eq 4, and noting that the summation over m gives a factor of $(2l+1)$:

$$\langle P_l(\hat{n}(0) \cdot \hat{n}(t)) \rangle = \frac{4\pi}{2l+1} \sum_{a,a'=-l}^l \sum_{\alpha,\beta=1}^{N_{Conformers}} \sum_{p_l=1}^{2l+1} c_{lp_l}^{\beta\alpha}(t) f_{l,a}^{(p_l)} f_{l,a'}^{(p_l)} Y_{la'}(\theta_\alpha, \phi_\alpha) Y_{la}^*(\theta_\beta, \phi_\beta) P_{eq}(\alpha) \tag{20}$$

The right hand side of the above equation can be simplified further by noting that the products $f_{l,a}^{(p_l)} f_{l,a'}^{(p_l)}$ are non-zero only for $a' = a \pm 2i$, $i \in \text{Integers}$, where $(a \pm 2i) \in \{-l, -l+1, \dots, +l\}$. In the following, the expression is explicitly evaluated for the case $l=2$. The

spherical harmonics and those $f_{2,a}^{(p_2)} f_{2,a'}^{(p_2)}$'s that are diffusion tensor-independent are

expressed explicitly (the $f_{2,a}^{(p_2)}$'s are diffusion tensor-dependent for $p_2 = 2, 3$), yielding the final result for the correlation function:

$$C(t) = \langle P_2(\hat{n}(0) \cdot \hat{n}(t)) \rangle = \sum_{\alpha,\beta=1}^{N_{Conformers}} \left\{ \begin{array}{l} c_{21}^{\beta\alpha}(t) \left\{ \frac{3}{4} \sin^2 \theta_\beta \sin^2 \theta_\alpha \sin(2\phi_\beta) \sin(2\phi_\alpha) \right\} \\ + c_{22}^{\beta\alpha}(t) \left\{ \begin{array}{l} \frac{3}{2} f_{2,2}^{(2)}(\{D_\beta\}) f_{2,2}^{(2)}(\{D_\alpha\}) \sin^2 \theta_\beta \sin^2 \theta_\alpha \cos(2\phi_\beta) \cos(2\phi_\alpha) \\ + \frac{\sqrt{3}}{2\sqrt{2}} \left[f_{2,2}^{(2)}(\{D_\beta\}) f_{2,0}^{(2)}(\{D_\alpha\}) \sin^2 \theta_\beta \cos(2\phi_\beta) (3 \cos^2 \theta_\alpha - 1) \right. \\ \left. + f_{2,0}^{(2)}(\{D_\beta\}) f_{2,2}^{(2)}(\{D_\alpha\}) \sin^2 \theta_\alpha \cos(2\phi_\alpha) (3 \cos^2 \theta_\beta - 1) \right] \\ + \frac{1}{4} f_{2,0}^{(2)}(\{D_\beta\}) f_{2,0}^{(2)}(\{D_\alpha\}) (3 \cos^2 \theta_\beta - 1) (3 \cos^2 \theta_\alpha - 1) \end{array} \right\} \\ + c_{23}^{\beta\alpha}(t) \left\{ \begin{array}{l} \frac{3}{2} f_{2,2}^{(3)}(\{D_\beta\}) f_{2,2}^{(3)}(\{D_\alpha\}) \sin^2 \theta_\beta \sin^2 \theta_\alpha \cos(2\phi_\beta) \cos(2\phi_\alpha) \\ + \frac{\sqrt{3}}{2\sqrt{2}} \left[f_{2,2}^{(3)}(\{D_\beta\}) f_{2,0}^{(3)}(\{D_\alpha\}) \sin^2 \theta_\beta \cos(2\phi_\beta) (3 \cos^2 \theta_\alpha - 1) \right. \\ \left. + f_{2,0}^{(3)}(\{D_\beta\}) f_{2,2}^{(3)}(\{D_\alpha\}) \sin^2 \theta_\alpha \cos(2\phi_\alpha) (3 \cos^2 \theta_\beta - 1) \right] \\ + \frac{1}{4} f_{2,0}^{(3)}(\{D_\beta\}) f_{2,0}^{(3)}(\{D_\alpha\}) (3 \cos^2 \theta_\beta - 1) (3 \cos^2 \theta_\alpha - 1) \end{array} \right\} \\ c_{24}^{\beta\alpha}(t) \left\{ \frac{3}{4} \sin(2\phi_\beta) \sin(2\phi_\alpha) \sin(\phi_\beta) \sin(\phi_\alpha) \right\} + c_{25}^{\beta\alpha}(t) \left\{ \frac{3}{4} \sin(2\phi_\beta) \sin(2\phi_\alpha) \cos(\phi_\beta) \cos(\phi_\alpha) \right\} \end{array} \right\} P_{eq}(\alpha) \tag{21}$$

The result of Eq 21 for the correlation function can then be inserted into the expression for

$$J(\omega) = \int_0^\infty C(t) \cos \omega t dt$$

the spectral density, which is the cosine Fourier transform of $C(t)$.

Finally, the spectral density occurs in the familiar equations for the relaxation times and the NOE for the case of relaxation mediated by carbon-proton dipole interaction and the carbon chemical shift anisotropy:

$$\frac{1}{T_1} = R_1 = \frac{d^2}{4} [J(\omega_H - \omega_C) + 3J(\omega_C) + 6J(\omega_H + \omega_C)] + c^2 J(\omega_C) \quad (22)$$

$$\frac{1}{T_2} = R_2 = \frac{d^2}{8} [4J(0) + J(\omega_H + \omega_C) + 3J(\omega_C) + 6J(\omega_H) + 6J(\omega_H + \omega_C)] + \frac{c^2}{6} [3J(\omega_C) + 4J(0)] \quad (23)$$

$$NOE = 1 + \frac{d^2}{4} \left(\frac{\gamma_H}{\gamma_C} \right) [6J(\omega_H + \omega_C) - J(\omega_C - \omega_H)] T_1 \quad (24)$$

$$d = \left[\frac{\mu_0 h \gamma_H \gamma_C}{8\pi^2 r_{CH}^3} \right], c = \left(\frac{\omega_C}{\sqrt{3}} \right) (\Delta) \quad (25)$$

In Eqns 22–25, ω_H and ω_C are the Larmor frequencies of 1H and ^{13}C respectively, μ_0 is the permeability of a vacuum, γ_H and γ_C are the magnetogyric ratios of 1H and ^{13}C , h is Planck's constant ($= 6.626 \times 10^{-34}$ J.sec), r_{CH} is the length of the C-H bond, and Δ is the chemical shift anisotropy (CSA). The effect of CSA tensor asymmetry is generally neglected in these expressions because it is small. The value chosen for r_{CH} in the following analysis was 1.1 Å and Δ was chosen to be 212 ppm. The choices for these parameters are the same as those in previous work²² and will not be further justified.

D. Solid-state models

In the following section, we will utilize motional models that have been derived from solid-state NMR experiments³⁸ to describe T_{1Z} , T_{1Q} relaxation measurements and the solid state lineshape. The observation of these motions was the motivation to develop the theory described in this manuscript, so we provide a brief summary of the models first (a more detailed summary is provided in our previous work²²).

Experimental results for the U38 base could be modeled through two motions around two independent axes: the first axis is perpendicular to the base plane and is termed a “base-libration” motion, and the best-fit to the data was obtained with a two-site jump with an amplitude of 8° ($\pm 4^\circ$) and a rate of 2.15×10^8 s⁻¹. The second, termed a “conformational exchange” motion, was interpreted as resulting from a bend in the upper helix of 9° and a twist of 15° about the upper helical axis at a rate of 1.38×10^6 s⁻¹. We note here that the original reference³⁸ quotes these values as a bend and a twist of 13° each, but one of the authors indicated that better fits were subsequently obtained with these new parameters. Because the solid-state experiments are insensitive to whether the twist is clockwise or counterclockwise, twist angles of either $\pm 15^\circ$ fit the solid-state NMR data equally well.

The models consist of equal populations of the two base-libration sites, as well as equal populations of the two conformers. For the analysis presented here, this means that $P_{eq}(\alpha)$ is 0.5 in all simulations.

The solid-state results were obtained for a hydration of 16 waters per nucleotide. The choice of this value was based on results which showed that the spectral densities of labeled sites did not change substantially for hydrations of 16 waters per nucleotide and higher.³⁹

3. Results

We present the results of applying Eqs 21 – 24 to calculate solution ^{13}C relaxation times for the HIV-1 Trans-Activation Response (TAR) RNA element.²² In order to apply the theory of this manuscript, molecular structures are required to define the exchanging conformers. According to the results of the solid state NMR data, we employed two sets of PDB files: (1) those available from our previous work,²² which reflect a modification of the bend angle of the upper helix relative to the lower helix about various axes perpendicular to the lower helix; and (2) new structures that were generated from the lowest energy TAR structure to include both a bend and a twist of the upper helix relative to lower helix (Figure 2). The structures shown in Figure 2 have been generated with twists of $\pm 15^\circ$ (Figure 2A corresponds to $+15^\circ$, and Figure 2B to -15°) applied to the upper helix about its own axis, in addition to the various bend angles. All structures considered here were generated from lowest energy structure of the unbound HIV-1 TAR RNA (PDB code 1ANR),²⁰ hereafter referred to as 1ANR-1, by rotating the upper helix relative to the lower helix about axes perpendicular to the lower helix, and, in the case of the second set, also twisting the upper helix about its axis of symmetry. In both cases, the bulge orientation was also kept fixed in its 1ANR-1 conformation. The second set also differs from the first set of structures (that was previously described) in the characterization of lower and upper helical axes, which was accomplished using the software package 3DNA.⁴⁰ The 1ANR-1 PDB file was rotated such that the z-axis corresponded with the lower helical axis. Any subsequent Euler rotation about the line of nodes would thus be perpendicular to the lower helix. The choice of the line of nodes within the plane perpendicular to the lower helix was made visually by selecting an orientation that resulted in the straightening of the upper helix relative to the lower helix. All Euler transformations were carried out manually by means of the UCSF Chimera program.⁴¹

To be consistent with the previous simulations, we limit our attention to bend angles $< 50^\circ$. This restriction is necessary because, as a result of keeping the bulge fixed, structures with bend angles greater than 50° introduce steric clashes between the upper helix and the bulge. Even the 40° and 50° structures in Figure 2A show close residue-residue encounters and many of the structures in Figure 2B contain steric clashes. More accurate models allowing for the rearrangement of the bulge may alleviate these problems, but these local details are very unlikely to affect the global properties of RNA that are studied in the present work.

In order to incorporate the base-libration motion, without any assumptions about the separation of the magnitudes of rates, each structure containing a particular site of the base-libration for each of the conformational exchange partners was treated as a separate conformer. Thus, a two-site base-libration coupled to a two-site conformational exchange process yielded four conformers to be used in Equation 18. The weighted rates $R_{\beta\gamma}$ were associated with either base-libration jump rates or conformational exchange jump rates, depending on which two conformers were being inter-related.

All simulations in this manuscript were conducted with essentially the same parameters used in the previous work. This included the input parameters for HYDRONMR,⁴² the public-domain program used in the calculation of the diffusion tensor eigenvalues and eigenvectors: an atomic element radius (AER) of 2.3 Å, a temperature of 298 K and solvent viscosity of $\eta_0 = 0.01096$ Poises (the viscosity of 99.9% D₂O at 25° C),⁴³ with the last two parameters determined based on the solution NMR experimental conditions.²⁴ It is worth

noting that no variation of the AER was considered in the current work (a discussion of the AER dependence of relaxation times can be found in the previous work²²), for the sake of brevity. The carbon-hydrogen bond length was set at 1.1 Å and the CSA parameter was taken to be 212 ppm. As in the previous work, we did not examine the heteronuclear NOEs in this work due to the minimal variation of values.

A. Comparison with Slow Exchange formalism

The solution T₁ and T₂ relaxation times were generated for the case of a two-site conformational exchange process between each of the rotated constructs and the original lowest energy unbound structure (1ANR-1), as motivated by solid-state NMR results.³⁸ The *a priori* probability of each conformer, $P_{eq}(\alpha)$, was taken to be 0.5, as mentioned in the previous section. Of course, this value of $P_{eq}(\alpha)$ was chosen purely based on the solid-state models and can be varied if so desired (this is not done in the current manuscript). The solid-state NMR results for U38 were well fit using a conformational exchange rate of 1.38×10^6 s⁻¹ between the two conformers, and the best-fit angular excursions consisted of a 9° bend and a twist 15° in amplitude in the upper helix. The solution times were simulated in our previous work under the assumption that this exchange rate between the two conformers, with different diffusion tensors, was substantially slower than the mean tumbling rate of the individual conformers and any other internal motion occurring in each of the two states. A slow exchange formalism was therefore proposed to this effect and implemented for multiple series of structures generated through rotations. In the current manuscript, we repeat the T₁ and T₂ simulations, but removing the assumption of slow exchange.

In the work published previously,²² the series of constructs were given the labels “90 degree series” and “30 degree series”, referring to the choice of the upper helix-rotation axis within the plane perpendicular to the lower helix. Therefore, the labels indicate that, in the second series, the upper helix was rotated through an axis that is 60 degrees away from that of the first series within the plane perpendicular to the lower helix. The rotation axes pass through the backbone at the hinge between U40 in the lower helix and C39 in the upper helix. The lower helix and bulge retain their conformations as observed experimentally in 1ANR-1.

We first applied the solid-state NMR-derived rate of 1.38×10^6 sec⁻¹ to Eq 18. The T₁ and T₂ values are shown in Figures 3A and 3B respectively, as a function of bend angle of the upper helix relative to its orientation in 1ANR-1 (the lower helix and bulge remain fixed), along with the corresponding relaxation times from the slow exchange formalism. The results for both the “90 degree series” (square symbols) and the “30 degree series” (circular symbols) are included in the same graphs. It must be noted that an important correction has been made to the results published previously in producing Figure 3. Namely, the relaxation times from that reference were mistakenly calculated with the x and y coordinates of the base-libration sites interchanged, an error that was discovered only after the publication of the manuscript. Given the small amplitude of the base-libration, the discrepancy in T₁ values was at most 4.3 ms and that in T₂ was less than 0.4 ms; these differences are small, so the previous conclusions would not change.

The residuals between the relaxation times obtained using the SE formalism and the general rate (GR) theory presented in Eqs. 22 and 23 ($T_{1,2}^{SE} - T_{1,2}^{GR}$) are shown in Figures 3C and 3D. For comparison, the experimental relaxation times are $T_1 = 354 \pm 3$ ms and $T_2 = 24.6 \pm 0.5$ ms.²⁴ The experimental times are indicated by the solid purple line, while the error bars are indicated by dashed blue lines. Also shown in grey in Figures 3A and 3B are the ±5% error regions for each of the relaxation times. These regions are included to provide room for additional systematic sources of uncertainty in the simulations arising from choices of the carbon-proton bond length and CSA, and are only visual guidelines.

As indicated by the residuals, the two calculations agree within the experimental error at the solid-state derived rate, supporting the SE formalism as the limiting case of the more general rate exchange theory. Conversely, this may be seen as confirming the behavior of the general rate theory in the infinitely slow limit that is familiar from other weighted population studies, such as those used for RDCs (see, for example, Blackledge⁴⁴ and Stelzer et al⁴⁵).

B. Rate dependence

We investigated the effect of changing the conformational exchange rate from $5 \times 10^5 \text{ s}^{-1}$ to $1 \times 10^9 \text{ s}^{-1}$ by applying the general rate theory to the structures from the previous work as well as to the new structures generated for this manuscript. Figure 4 shows the T_1 (Fig. 4A) and T_2 (Fig. 4B) dependence on the conformation rate for the “90 degree series,” while Figure 5 shows the T_1 (Fig. 5A) and T_2 (Fig. 5B) dependence on the conformation rate for the “30 degree series.” It can be seen that deviations from the slow limit values become apparent for rates of $1 \times 10^7 \text{ s}^{-1}$ and higher, the regime where the rates of rotational diffusion, base libration and conformational exchange become sufficiently close to have a cumulative impact upon the relaxation times. Due to the small amplitude of the base libration, the overlap of rates between tumbling and conformational exchange is likely to be the more significant determinant of the rate of relaxation.

Another important feature of these results is that the changes in relaxation times with increases in conformational exchange rates up to $1 \times 10^7 \text{ s}^{-1}$ occur only for conformational bend angles $> 30^\circ$. In other words, the amplitude of the change in the structure of the molecule needs to be substantial in order for the change to be reflected in the relaxation times. Exchange between structures that have similar diffusion tensors will understandably be difficult to discern. It is clear, however, that upon increasing the rate even further, even structures at lower bend angles begin to deviate from the slow limit behavior, implying that the effect of the conformational rate increase can amplify even small differences in diffusion tensors (note, for example, the 20° bend angle structure for rates $< 5 \times 10^7 \text{ s}^{-1}$ in Figures 5A and 5B).

In addition, the relaxation times for an exchange rate of $1 \times 10^9 \text{ s}^{-1}$, a rate higher than the base libration and tumbling observed experimentally, are also worth noting. While the trend of decreasing T_1 values and increasing T_2 values continues even up to this point, it will be seen in the following subsection that this trend is not monotonic for the T_1 times and eventually reverses itself at higher rates.

Concerning the experimental solution relaxation data, there is an interdependence of the values of the two parameters of exchange rate and bend angle that provide the closest fit to the data. Thus, for rates less than or equal to $1 \times 10^7 \text{ s}^{-1}$, the “90 degree series” graphs show reasonable agreement for all bend angles $< 50^\circ$. For rates $> 1 \times 10^7 \text{ s}^{-1}$, structures with bend angles $> 30^\circ$ begin to deviate from the experimental values. The “30 degree series” graphs are more restrictive in the fit parameters, where an increase in rate results in a decrease in the upper limit of the bend angles that fit the data. Higher bend angles of between 40° and 50° are inconsistent with the experimental data for almost all rates considered.

We repeated the same calculations using the models in Figure 2, whose upper helices are rotated by $\pm 15^\circ$ about their own axes in addition to the bend angles $< 50^\circ$. The series of models in Figure 2A will hereafter be referred to as the “Tw15 series,” and those in Figure 2B as the “Tw-15 series.” The results for both series are shown in Figures 6 (“Tw15 series”) and 7 (“Tw-15 series”).

Before describing the results, it is essential to note that the structure with a 0° bend angle is not the 1ANR-1 structure. In order to consider the effect of applying a twist alone to the upper helix, this initial structure was generated with a $+15^\circ$ or -15° twist, and subsequently averaged with 1ANR-1. Moreover, the 1ANR-1 model used in this manuscript was rotated relative to the 1ANR-1 used in the previous work, as a result of the different characterization of the helical axes with 3DNA in our current work, and with having to align the lower helix with the z-axis. Ideally, this overall rotation should not affect the diffusion eigenvalues. However, HYDRONMR, the program used to calculate the eigenvalues, outputs two slightly different sets of diffusion eigenvalues, with the result that the relaxation times changed slightly (on the order of 5 ms for T_1 and 0.3 ms for T_2). We surmise that this difference is due to discrepancies in the extrapolation of the diffusion eigenvalues towards zero bead size and to rounding-off errors. This discrepancy was lessened by using many more points in the extrapolation process, but, in order to match the results of the previous work, the same lower number of points (6 extrapolation points) was used here as well.

Figure 6A reports the simulated T_1 values for the “Tw15 series,” that fit the experimental data best for bend angles between 10° and 30° . Bend angles between 10° and 30° fit the data for exchange rates $<1 \times 10^7 \text{ s}^{-1}$, while for higher rates the best-fit range is confined to angles between 10° and 20° . The simulated T_2 values in Figure 6B accord with the data for bend angles $< 30^\circ$ for rates $< 1 \times 10^7 \text{ s}^{-1}$. Higher rates fit the experimental data only for bend angles $> 20^\circ$. As mentioned before, due to uncertainties in the calculation of the diffusion eigenvalues, these ranges may have to be altered slightly, but there does seem to be a trend of lower rates increasing the range of bend angles that match the data. Moreover, the simulated relaxation times seem to better fit the experimental values for lower bend angles in general. Considering the results for the “Tw-15 series” in Figures 7A and 7B, for rates $< 1 \times 10^7 \text{ s}^{-1}$, models with bend angles between 10° and 20° fit the data better, while for higher rates the best-fit bend angles are limited to $< 10^\circ$.

In an attempt to separate the various combinations of parameters that fit the experimental data, we must utilize the findings of other experiments. Since the models considered here are based on solid-state NMR data, we can check against the best-fit parameters mentioned in Section 2D. Ignoring for a moment the twist of the helix, Figures 4 and 5 show that the T_1 values for the solid-state bend and rate parameters are slightly outside of the experimental error bars, while they are within the error bars for the T_2 times. Given that there may be round-off errors in the evaluation of diffusion tensors, the discrepancy in the T_1 values may not be significant.

Considering the twist angles as well, for the “Tw15 series” Figure 6 shows that the simulated T_1 is outside the error bars once again, and so are the T_2 's, although the discrepancy for the latter is fairly small. However, a much better fit is obtained for the “Tw-15 series” (Figure 7) using the solid-state parameters, with the T_1 value being just outside the experimental errors bars and the T_2 value well within them. While this may be construed as a means of breaking the degeneracy of the solid-state results with respect to the direction of twist of the upper helix, we reiterate that there are errors due to steric clashes in the models used and uncertainties in the other free parameters in the problem. The tentative conclusion is that it is plausible that the solid-state parameters continue to be valid under solution sample conditions: previous studies of the RNA as a function of hydration have shown that relaxation times remain fairly constant above a hydration of $W = 16$.³⁹ Again, we have not repeated our previous studies of the impact of the choice of the hydrodynamic bead radius (or, atomic element radius AER) on the simulations, and a consideration of the appropriate value of this parameter also seems essential.

C. T_1 turnover

Having observed the changes in relaxation times as a function of the conformational exchange rate up to a value $1 \times 10^9 \text{ s}^{-1}$, we examined if the trend continued indefinitely to even higher rates of conformational exchange. To that end, we simulated relaxation times for all the four sets of structures used in Figures 4 – 7, with an exchange rate of $1 \times 10^{10} \text{ s}^{-1}$. The T_1 graph is shown in Figure 8A. Here the dependence on the bend angle has been completely inverted, with an increase in T_1 for increasing bend angles. The T_1 values have swung over to much higher values, signaling that there is a turnover point in the range between $1 \times 10^9 \text{ s}^{-1}$ and $1 \times 10^{10} \text{ s}^{-1}$, where the T_1 times go through a minimum and reverse their dependence on exchange rate. To localize the minimum further, we also calculated the T_1 for a rate of $5 \times 10^9 \text{ s}^{-1}$. The results are shown in Figure 8B. As the graphs seem to have already crossed the turnover point from a downward trend to an upward one, the T_1 minimum is seen to be at slightly less than $5 \times 10^9 \text{ s}^{-1}$.

The T_2 graphs for rates of $1 \times 10^{10} \text{ s}^{-1}$ and $5 \times 10^9 \text{ s}^{-1}$ are shown in Figures 9A and 9B respectively. Figure 9A shows that, unlike the T_1 values, the T_2 times have not changed their trend. A comparison of the times at the two rates shows, however, that the difference in times is fairly small. Upon testing the values of T_2 for the 50° models (which showed the most dramatic changes), we observe that an increase of the rate up to $1 \times 10^{12} \text{ s}^{-1}$ (data not shown) caused only small changes in the relaxation times relative to the values at $5 \times 10^9 \text{ s}^{-1}$. The T_2 times seem to have reached their fast time limits by the time the T_1 values turn around.

D. Twist angle dependence

The “Tw15 series” and the “Tw-15 series” shown in Figure 2 represented two sets in a series of models that were constructed with various degrees of twist applied to the upper helix relative to its orientation in 1ANR-1. The twist angles that were applied range from -60° to $+60^\circ$ in 15° increments. Again, the initial structure is not the 1ANR-1 structure, but one with the upper helix rotated through the twist angle associated with that particular series, and all models, including this 0° bend angle model, are averaged with the 1ANR-1 structure to produce the results that follow.

Relaxation times have been calculated for the twist angle models using the solid-state exchange rates of $1.38 \times 10^6 \text{ s}^{-1}$. For clarity, the data for positive twist angles and negative twist angles have been separated into distinct graphs. The T_1 relaxation times are shown in Figure 10, with the positive twist angle data in Figure 10A and that for negative twists in Figure 10B. With few exceptions, changes in the twist angle relative to the 1ANR-1 are directly proportional to changes in the T_1 time. Correspondingly, there is an increase in the best-fit bend angles with an increase in twist angle. For example, the 0° twist angle structures match the experimental data for bend angles less than 20° . However, by changing the twist in the upper helix to 45° , the range of best-fit bend angles shifts to $20^\circ < \theta_{\text{best-fit}} < 50^\circ$. Figure 11A and 11B show the corresponding T_2 simulations. There is an inverse relationship between twist angles and T_2 values, barring some instances which do not follow this simple trend. As with the T_1 values, this leads to the best-fit twist and bend angles being correlated.

The physical origin of this correlation must be understood by considering changes in the diffusion tensor and the orientation of the local C–D bond relative to the diffusion tensor frame. Since the helices of the molecule are not perfectly axially-symmetric, it is possible that changes in the diffusion tensor eigenvalues and bond orientation relative to the tensor eigenvectors arising from a twist in the upper helix for a given bend angle mimic those for a different set of twist and bend angles. Alternately, it is also possible that the relationship

between the diffusion tensor eigenvalues and the bond orientation on the one hand, and the ensuing relaxation times on the other is simply not one-to-one. The relaxation times T_1 and T_2 are merely two numbers that are obtained analytically as a combination of several parameters, and what we observe in Figures 10 and 11 may be a manifestation of the degeneracy of the parametric landscape with respect to the relaxation times.

Using the solid-state values for the parameters, it can be seen from Figures 10A and 11A that the structure with a positive twist of 15° does not fit the T_1 experimental value, but almost fits the T_2 value. On the other hand, if we consider the -15° twist structure in Figures 10B and 11B, we see that the experimental T_1 value is very close to being fit and T_2 value fits well within the error bars. Since the solid-state experiments are unable to distinguish the sense of rotation, solution relaxation times may help to break this degeneracy, if the values of other parameters are determined independently.

4. Discussion

The theoretical method and results presented in this manuscript aim to introduce a new method of applying molecular motional models with atomic-level detail derived from other techniques to solution NMR relaxation results, and include the possibility of motions that alter the diffusion tensor. We also have extended the TAR-specific results presented in the previous work,²² by removing the key assumption of an infinitely slow exchange between conformers. With regards to the first goal, the applicability of the current approach extends beyond the solid-state/solution NMR application described here, and can be expanded to corroborate any type of motion inferred from other experiments, provided molecular structures are available. Moreover, it may be possible to simulate further time-dependent, diffusion-averaged solution-state observables that can be described in terms of correlation functions of Wigner rotation matrices, in addition to relaxation rates, simply by utilizing the transition probability (Equation 17) in the expression analogous to Equation 4.

In our recent work,²² we referred to the ssNMR-based models for the residues U23 and U25 described in a previous article,³⁸ models which include local motions that were close to the overall tumbling timescale. While an inclusion of simulations of these two bases would support the generality of the theory presented here, these two residues occur in the trinucleotide bulge region of TAR-RNA and any description of their dynamics would necessitate an understanding of changes in the bulge configuration. As mentioned in Section 3, the bulge is assumed to be rigid in our current structure manipulations. In order to reasonably simulate such motions, we would need to obtain a set of atomic-level orientations of the bulge residues and the concurrent helix configurations. Such studies require new approaches, one of which is currently being evaluated.

Along similar lines, we emphasize the requirement of detailed atomic-level structures. In the current manuscript we have used 1ANR-1 as the starting structure for all of our simulations. However, the use of any one of the 20 lowest energy structures reported under the PDB code 1ANR²⁰ would result in significantly different constraints on parameters. We evaluated the impact of a different choice of initial structure by calculating the relaxation times for the first five lowest energy structures (1ANR 1–5) tumbling as single conformers, without internal motion. In the original reference²⁰ energy is quantified by the energy of NOE constraint violations, and these first few structures do not differ greatly in energy. The maximum difference in T_1 was approximately 80 ms and in T_2 was about 5 ms (both between the results for 1ANR-2 and 1ANR-4). The discrepancies arise from the fact that the structures 1ANR 1–20 show significant variations in relative helix placement, and relative base orientations, even within base pairs. These substantial differences motivate searches for well-established energy-minimum structures, especially given that computational capacity

has improved vastly since the original publication of the structures 15 years ago. However, the methodology and the qualitative arguments made herein still hold for any given choice of initial structure, and given recent trends towards more accurate molecular structures this contributor to uncertainty is likely to be removed in the near future.

The work presented here includes a re-derivation of the results of Favro,³¹ Huntress³² and Freed³³ and attempts to incorporate the discrete-jump formalism described by Wong, Case and Szabo.³⁷ We have applied this formalism to a molecule, HIV-I TAR RNA, where many of the structures deviate significantly from cylindrical idealizations. This application of the formalism, the second central objective of the current manuscript, has shown that it is possible to fit the solution experimental data given reasonable choices of the available parameters. We already considered the impact of changing the conformational bend angle, the atomic element radius (AER, representing the size of the hydrodynamic beads that are used to represent each atom) and the direction of helical bending in previous work. Additional parameters considered here are the rate of conformational exchange, and the twist angle about the upper helix.

Although discussed previously,²² it bears reminding that the ssNMR models³⁸ used as a basis for the simulations in this manuscript report only on the upper helix motions. No site labels in the lower helix were considered at the time so that information on the relative motions of the two helical domains could not be acquired. This motivated us to explore a wider range of inter-helical bend and twist angles than suggested by ssNMR models alone, to account for possible lower helical motions.

Based on our new analysis, it is worthwhile to revisit the comparison with the work of Zhang, Al-Hashimi and co-workers^{21,25} that were made previously.²² An order tensor analysis in Zhang et al 2007²¹ reported an average upper helix bend of 25° relative to an elongated lower helix and an average lower helix bend of 54° relative to an elongated upper helix, with the difference between the two results being ascribed to differing twist motions of the two helices. As described before, ssNMR models³⁸ corroborate these collective twisting and bending motions. The quoted results for the average orientations in Zhang et al 2007 are accompanied by a significantly lowered level of order for both helices, indicating very large amplitude helix motions (see also Zhang et al 2008⁴⁶). A direct comparison of our results with the above average orientations is not possible as the order tensor elements probe the average inter-helical bend, while the bend angles considered herein are measured with respect to the lowest energy structure 1ANR-1. As an initial attempt at comparing the two sets of angles, we calculated the approximate symmetry axes of the upper and lower helices using 3DNA⁴⁰ and found an inter-helical bend of 75° for 1ANR-1. Given the equal populations of the two conformers considered here, this would imply a total helical bend relative to the 1ANR-1 structure of about 100° for an average of 25° (i.e. an amplitude of 2×(75° - Average angle)) and about 40° for an average angle of 54°. We did not consider bend angles as large in magnitude as 100°, but it is conceivable that some combinations of the parameters, including the exchange rate, could allow this value to be fit. The amplitude of 40° can be fit to the experimental data if we assume the ssNMR exchange rate of 1.38×10^6 s⁻¹ and twist angles of 30°, θ_{twist} 60° and θ_{twist} around -45°. Other AERs and directions of helical reorientation might also allow matches between the two sets of results.

Zhang et al 2007 also reports the results of a three-conformer ensemble study suggesting an overall helical bend of 94°, an upper helical twist of 110° and a lower helical twist of 53°. While we did not extend our analysis to bend angles of that magnitude, nor to upper helical twists greater in magnitude than 60°, it is conceivable, based on the trends in Figures 10 and 11 that the Zhang et al 2007²¹ values could fit our solution data.

However, the time scale of domain motions quoted in Zhang et al 2006²⁵ is 1.5–1.9 ns (rate $\sim 5\text{--}7 \times 10^8 \text{ s}^{-1}$) and that differs significantly from the ssNMR time scale of 725 ns (rate = $1.38 \times 10^6 \text{ s}^{-1}$). Figures 4 – 7 of the current manuscript show that using the higher rates from Zhang et al 2006²⁵ would preclude bend angles greater than about 30° for any of the directions of helical reorientation considered here. Thus, given particular choices of the parameters, the solution results may be reconciled with each other, although the discrepancy of the time scale in Zhang et al 2006²⁵ with the ssNMR time scale still remains. However, given the fact that the Zhang et al 2006 result was produced by a Model-free analysis, the rate of motions captured is necessarily faster than the overall tumbling rate, thereby precluding the inclusion of any slower conformational motions on the timescales considered here. Indeed, the RDC-based analysis in Zhang et al 2007 confirms the existence of larger domain motions (leading to a lower degree of order) potentially occurring on timescales up to milliseconds (to which an RDC would be sensitive). The ssNMR results are also able to capture motions on longer timescales, and previously³⁸ a model-dependent approach was used to pin-point a particular exchange rate. Thus, the discrepancy mentioned above may be attributed to the greater sensitivity of the ssNMR approach to slower timescales of motion.

Multiple sets of parameters can produce the same values of the relaxation times: this degeneracy must be broken by an independent experimentally-driven assessment of the parameters. For example, we may take the solid-state best-fit parameters as being relevant even under solution conditions, especially given that hydration-based studies show a relatively flat hydration dependence of the relaxation times at high hydration levels.³⁹ In this case, we can fix the conformational bend angle to 9°, the twist angle to 15° and the conformational exchange rate at $1.38 \times 10^6 \text{ s}^{-1}$. The evaluation of goodness-of-fit of the ensuing solution simulations has been made in Section 3. This leaves the AER and direction of helical bending as free parameters to be optimized. Our current value of an AER of 2.3 Å provides a tumbling correlation time $\tau_c^{rot} = (6D)^{-1}$ (where D is the trace of the rotational diffusion tensor) of 6.4 ns for the 1ANR-1 conformer alone, which accords well with the Model-free-derived value of 5.9 ns for free TAR as reported in Bardaro et al.²⁴ While the experimental time is averaged over all conformational states accessed by free TAR, the remarkable similarity in the time scale provides some independent corroboration of the choice of AER. Furthermore, detailed hydration studies of nucleic acids may provide more independent estimates of the impact of various hydration patterns, if we can solve for diffusion tensors using explicit water molecules. The direction of helical bending is physically determined by the backbone torsion degrees of freedom and the inter-residue interactions (including steric clashes), and these properties may be studied using molecular dynamics simulations and energy minimization studies. Since the bending of the upper helix is associated with changes in the bulge configuration, we have begun investigating the possibility of simulating both helix bending and the bulge residue orientations using the aforementioned techniques.

5. Conclusions

In this manuscript we have presented a method of testing proposed motional models of macromolecules in solution conditions by simulating solution NMR T₁ and T₂ relaxation times. Specifically, we have made use of available solid-state NMR-derived models to determine the types of motions experienced by the upper helix of the HIV-1 TAR RNA molecule. In addition to showing that the solid-state NMR (at a hydration of 16 waters per nucleotide) dynamic parameters provide reasonable fits to the solution relaxation data, we have also made an exploration of the dependence of the relaxation times on variations in the dynamic parameters. For future studies on this system or on RNA in general, the analyses conducted herein can serve as a means of reducing the large motional parameter space, and

also provide qualitative insight regarding trends in parametric correlations. We believe that the method is generally applicable to a variety of macromolecules and can be extended easily to include new observables, thereby bridging gaps between multiple experimental techniques.

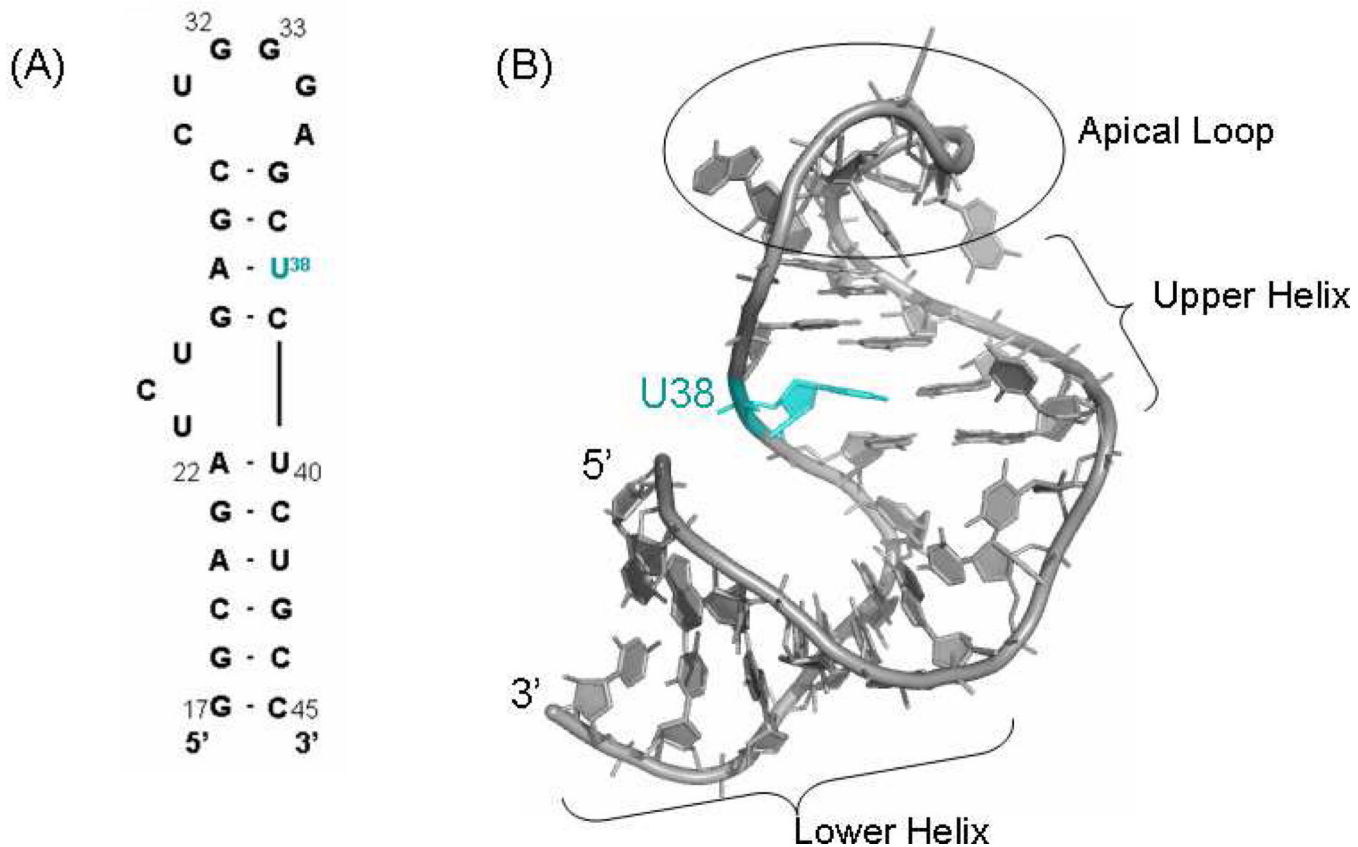
Acknowledgments

This work was supported by grants from the NSF (MCB-0642253) and NIH (RO1-EB03152) to G.P.D. and G.V. We are grateful to Michael Bardaro for providing the TAR relaxation data and their error analysis and to Jason Ash and Dorothy Echodu for helpful discussions and suggestions.

References

1. Dethoff EA, Hansen AL, Musselman C, Watt ED, Andricioaei I, Al-Hashimi HM. *Biophys. J.* 2008; 95:3906–3915. [PubMed: 18621815]
2. Shajani Z, Deka P, Varani G. *Trends Biochem. Sci.* 2006; 31:421–424. [PubMed: 16815707]
3. Koplin J, Mu Y, Richter C, Schwalbe H, Stock G. *Structure.* 2005; 13:1255–1267. [PubMed: 16154083]
4. Al-Hashimi HM. *Biopolymers.* 2007; 86:345–347. [PubMed: 17597469]
5. Aboul-ela F, Karn J, Varani G. *J. Mol. Biol.* 1995; 253:313–332. [PubMed: 7563092]
6. Hennig M, Williamson JR. *Nucleic Acids Res.* 2000; 28:1585–1593. [PubMed: 10710425]
7. Brodsky AS, Williamson JR. *J. Mol. Biol.* 1997; 267:624–639. [PubMed: 9126842]
8. Long KS, Crothers DM. *Biochemistry.* 1999; 38:10059–10069. [PubMed: 10433713]
9. Puglisi JD, Tan R, Calnan BJ, Frankel AD, Williamson JR. *Science.* 1992; 257:76–80. [PubMed: 1621097]
10. Razga F, Zacharias M, Reblova K, Koca J, Sponer J. *Structure.* 2006; 14:825–835. [PubMed: 16698544]
11. Falb M, Amata I, Gabel F, Simon B, Carlomagno T. *Nucleic Acids Res.* 2010; 38:6274–6285. [PubMed: 20466811]
12. Greenleaf WJ, Frieda KL, Foster DAN, Woodside MT, Block SM. *Science.* 2008; 319:630–633. [PubMed: 18174398]
13. Stoddard CD, Montange RK, Hennelly SP, Rambo RP, Sanbonmatsu KY, Batey RT. *Structure.* 2010; 18:787–797. [PubMed: 20637415]
14. Klimasauskas S, Kumar S, Roberts RJ, Cheng XD. *Cell.* 1994; 76:357–369. [PubMed: 8293469]
15. Shajani Z, Varani G. *Biochemistry.* 2008; 47:7617–7625. [PubMed: 18578505]
16. Pederson K, Meints GA, Shajani Z, Miller PA, Drobny GP. *J. Am. Chem. Soc.* 2008; 130:9072–9079. [PubMed: 18570423]
17. Bothe JR, Lowenhaupt K, Al-Hashimi HM. *J. Am. Chem. Soc.* 2011; 133:2016–2018. [PubMed: 21275369]
18. Puglisi JD, Chen L, Frankel AD, Williamson JR. *Proc. Natl. Acad. Sci. U. S. A.* 1993; 90:3680–3684. [PubMed: 7682716]
19. Long KS, Crothers DM. *Biochemistry.* 1995; 34:8885–8895. [PubMed: 7612630]
20. Aboul-ela F, Karn J, Varani G. *Nucleic Acids Res.* 1996; 24:3974–3981. [PubMed: 8918800]
21. Zhang Q, Stelzer AC, Fisher CK, Al-Hashimi HM. *Nature.* 2007; 450:1263–1267. [PubMed: 18097416]
22. Emani PS, Olsen GL, Echodu DC, Varani G, Drobny GP. *J. Phys. Chem. B.* 2010; 114:15991–16002. [PubMed: 21067190]
23. Shajani Z, Varani G. *Biopolymers.* 2007; 86:348–359. [PubMed: 17154290]
24. Bardaro MFJ, Shajani Z, Patora-Komisarska K, Robinson JA, Varani G. *Nucleic Acids Res.* 2009; 37:1529–1540. [PubMed: 19139066]
25. Zhang Q, Sun X, Watt ED, Al-Hashimi HM. *Science.* 2006; 311:653–656. [PubMed: 16456078]
26. Zhang Q, Al-Hashimi HM. *RNA.* 2009; 15:1941–1948. [PubMed: 19776156]

27. Tugarinov V, Liang Z, Shapiro YE, Freed JH, Meirovitch E. *J. Am. Chem. Soc.* 2001; 123:3055–3063. [PubMed: 11457016]
28. Olsen GL, Echodu DC, Shajani Z, Bardaro MFJ, Varani G, Drobny GP. *J. Am. Chem. Soc.* 2008; 130:2896–2897. [PubMed: 18275190]
29. Perrin F. *Le Journal de Physique.* 1936; 7:1–11.
30. Woessner DE. *J. Chem. Phys.* 1962; 37:647–654.
31. Favro LD. *Phys. Rev.* 1960; 119:53–62.
32. Huntress WT. *J. Chem. Phys.* 1968; 48:3524–3533.
33. Freed JH. *J. Chem. Phys.* 1964; 41:2077–2083.
34. Jackson, JD. *Classical Electrodynamics.* 3rd ed.. John Wiley & Sons, Inc.; 1998.
35. Rose, ME. *Elementary Theory of Angular Momentum.* New York: Wiley; 1957.
36. Tinkham, M. *Group Theory and Quantum Mechanics.* New York: McGraw-Hill; 1964.
37. Wong V, Case DA, Szabo A. *Proc. Natl. Acad. Sci. U. S. A.* 2009; 106:11016–11021. [PubMed: 19541602]
38. Olsen GL, Bardaro MFJ, Echodu DC, Drobny GP, Varani G. *J. Am. Chem. Soc.* 2010; 132:303–308. [PubMed: 19994901]
39. Olsen GL, Bardaro MFJ, Echodu DC, Drobny GP. *J. Biomol. NMR.* 2009; 45:133–142. [PubMed: 19669102]
40. Lu XJ, Olson WK. *Nucleic Acids Res.* 2003; 31:5108–5121. [PubMed: 12930962]
41. Pettersen EF, Goddard TD, Huang CC, Couch GS, Greenblatt DM, Meng EC, Ferrin TE. *J. Comput. Chem.* 2004; 25:1605–1612. [PubMed: 15264254]
42. de la Torre JG, Huertas ML, Carrasco B. *J. Magn. Reson.* 2000; 147:138–146. [PubMed: 11042057]
43. Millero FJ, Dexter R, Hoff E. *J. Chem. Eng. Data.* 1971; 16:85–87.
44. Blackledge M. *Progress in Nuclear Magnetic Resonance Spectroscopy.* 2005; 46:23–61.
45. Stelzer AC, Frank AT, Bailor MH, Andricioaei I, Al-Hashimi HM. *Methods.* 2009; 49:167–173. [PubMed: 19699798]
46. Zhang Q, Al-Hashimi HM. *Nat. Meth.* 2008; 5:243–245.

**Figure 1.**

A) Sequence and secondary structure of the HIV-1 TAR RNA construct used in this study. The U38 residue, which was deuterium labeled at the H5 and H6 sites for solid-state NMR studies and is the subject of the present theoretical study, is highlighted in cyan. Watson-Crick base pairings are shown with short dashes. B) Lowest energy free TAR structure 1ANR. The U38 residue is shown in cyan. The lower helix, upper helix and apical hairpin loop regions are also indicated. Hydrogen atoms have been removed from the figure for clarity.

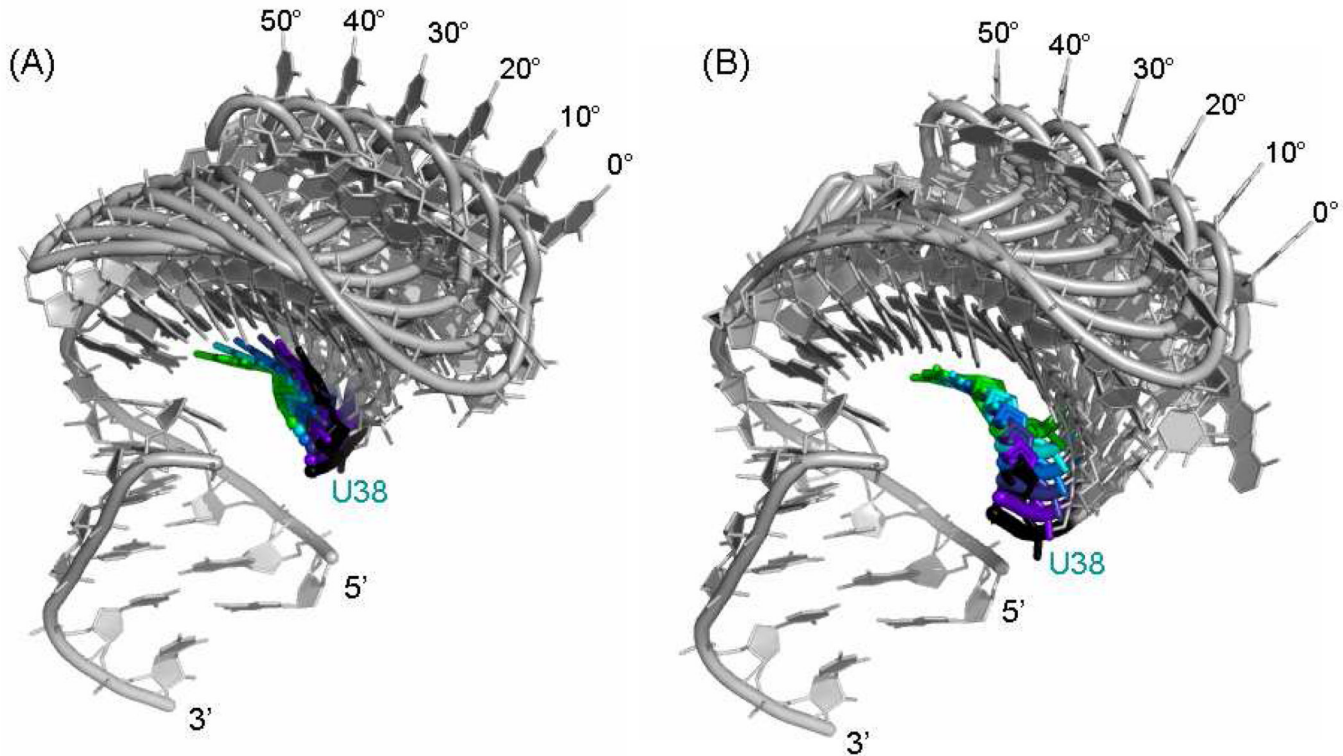
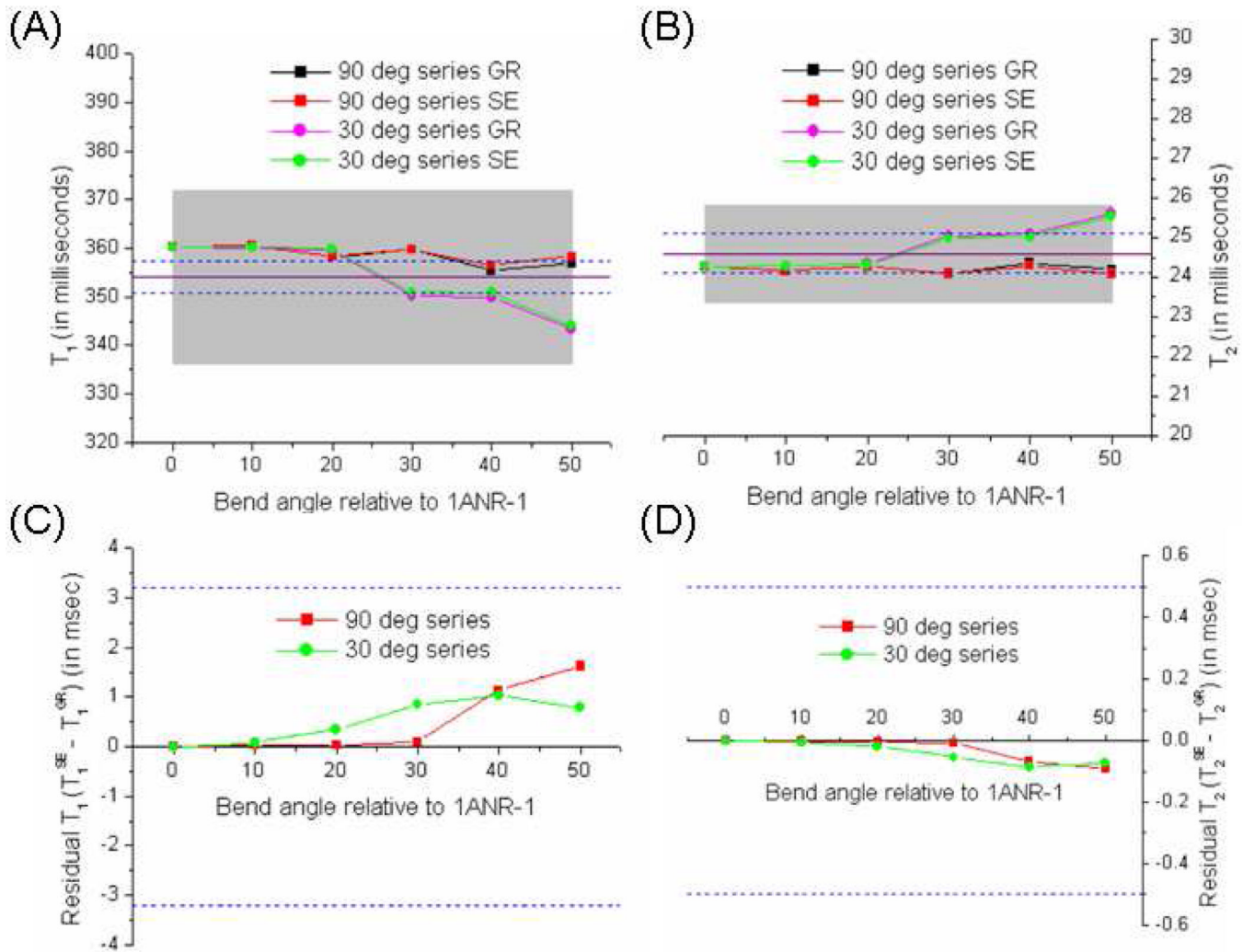
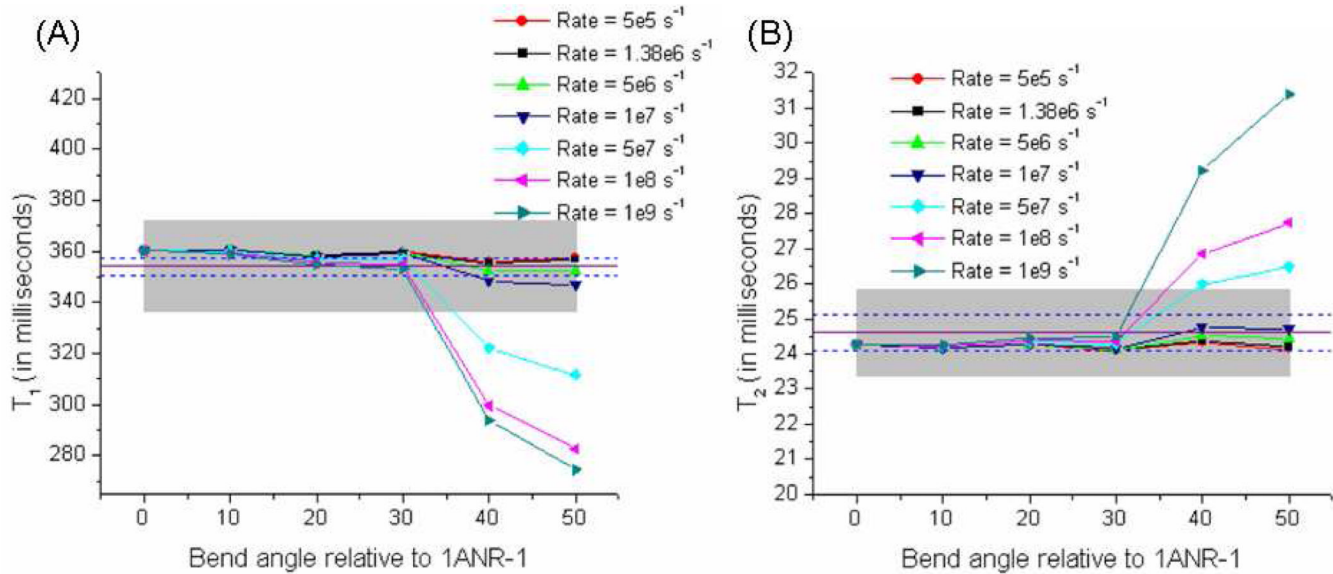


Figure 2.

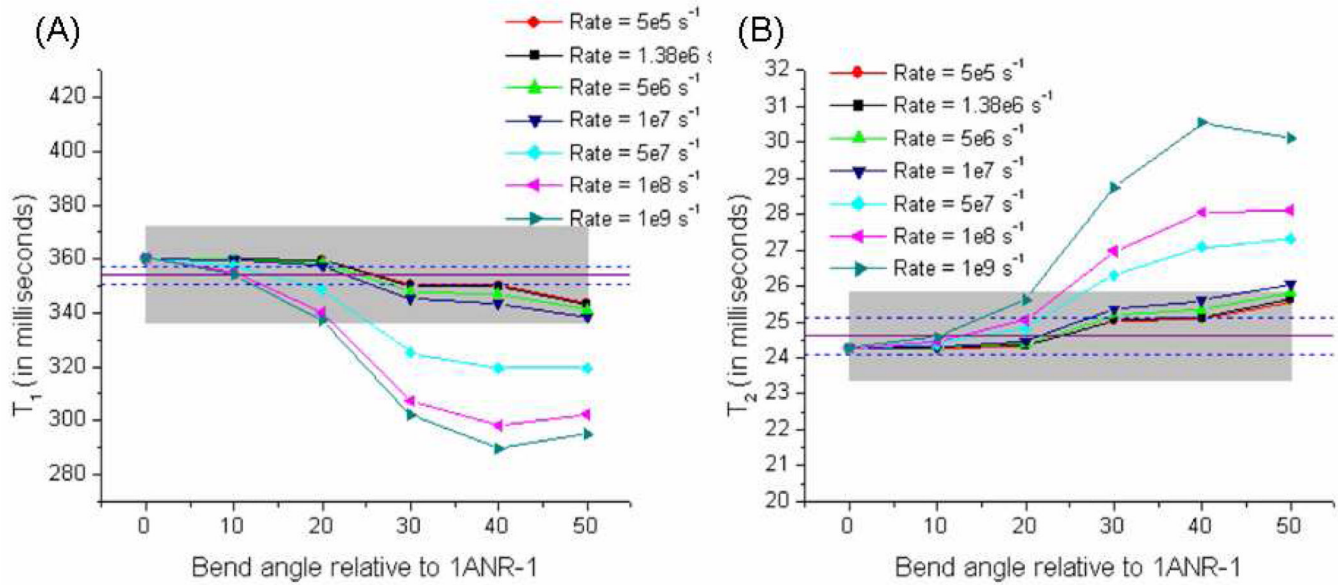
Models of TAR generated from the lowest energy TAR RNA structure (1ANR-1) by bending the upper helix relative to its orientation in 1ANR-1. The bend angles are indicated next to the corresponding structures. (A) These models have a twist of 15° applied to the upper helix in addition to the reported bend angles; these structures are denoted as the “Tw15 series.” (B) These models have a twist of -15° applied to the upper helix in addition to the bend angles; they are denoted as the “Tw-15 series.” The labeled U38 base is shown in colors ranging from black (0°) to green (50°). The hydrogen atoms and the C39 residues have been removed from both figures for greater clarity.

**Figure 3.**

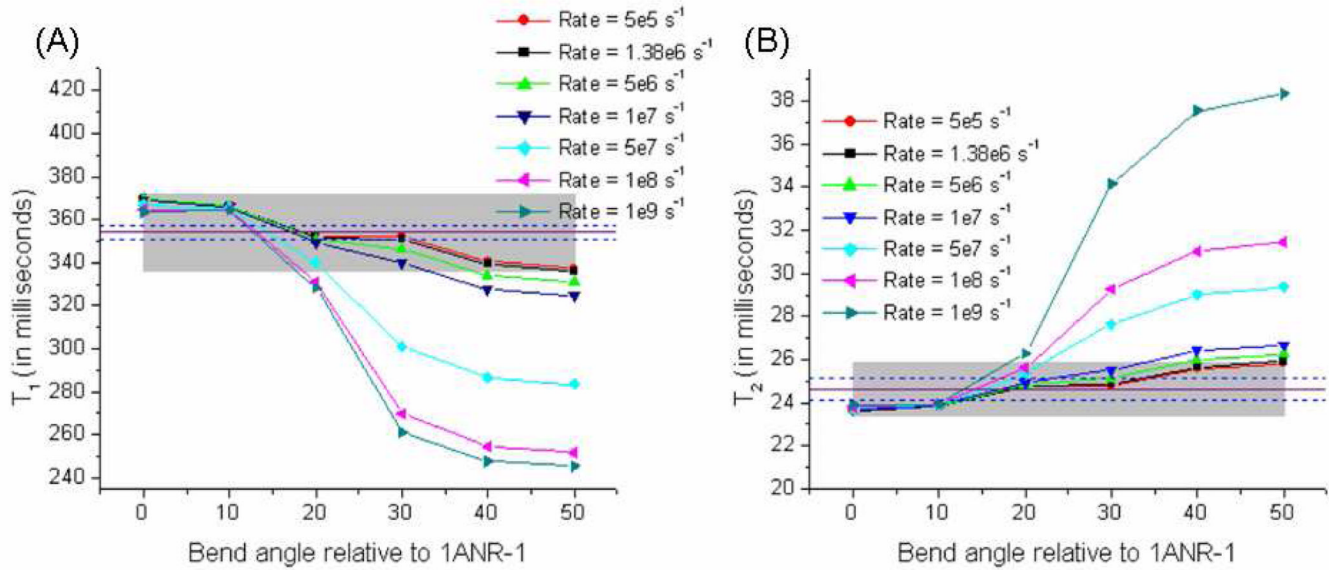
Comparison of relaxation times calculated using slow exchange (SE) and general rate (GR) formalisms. (A) T_1 times for the “90 degree series” and “30 degree series.” (B) T_2 times for the “90 degree series” and “30 degree series.” Experimental values are marked by solid purple lines, and the error bars are indicated by dashed blue lines; also shown in grey is the $\pm 5\%$ error region. The experimental relaxation times are: $T_1^{\text{Expt.}} = 354 \pm 3$ ms, and $T_2^{\text{Expt.}} = 24.6 \pm 0.5$ ms. The residuals ($T_{1,2}^{\text{SE}} - T_{1,2}^{\text{GR}}$) are shown in (C) (for T_1) and (D) (for T_2). The experimental error bars are shown again as dashed blue lines.

**Figure 4.**

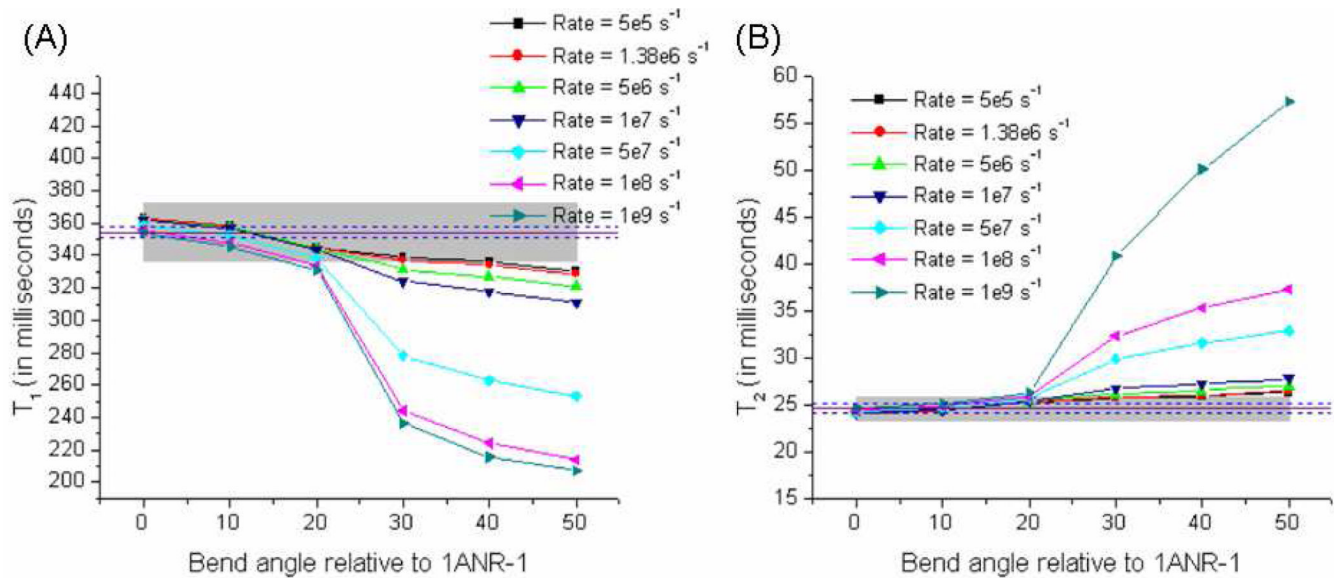
Relaxation times vs. bend angle for structures within the “90 degree series,” considering various exchange rates from $5 \times 10^5 \text{ s}^{-1}$ to $1 \times 10^9 \text{ s}^{-1}$: (A) T_1 times; and (B) T_2 times. Experimental values are marked by solid purple lines, and the error bars are indicated by dashed blue lines. The experimental relaxation times are: $T_1^{\text{Expt.}} = 354 \pm 3 \text{ ms}$, and $T_2^{\text{Expt.}} = 24.6 \pm 0.5 \text{ ms}$. Also shown in grey is the $\pm 5\%$ error region.

**Figure 5.**

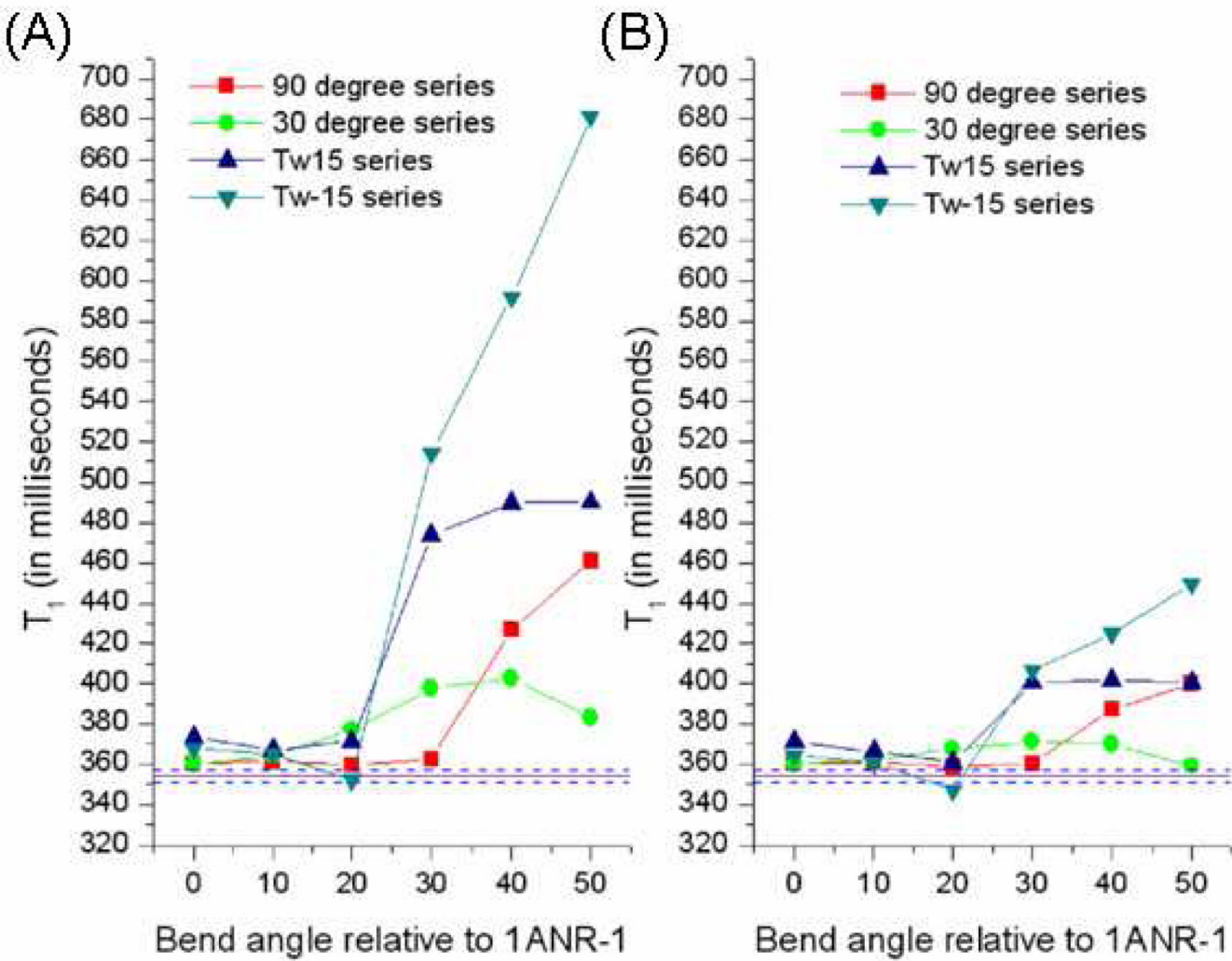
Relaxation times vs. bend angle for structures within the “30 degree series,” considering various exchange rates from $5 \times 10^5 \text{ s}^{-1}$ to $1 \times 10^9 \text{ s}^{-1}$: (A) T_1 times; and (B) T_2 times. Experimental values are marked by solid purple lines, and the error bars are indicated by dashed blue lines. The experimental relaxation times are: $T_1^{\text{Expt.}} = 354 \pm 3 \text{ ms}$, and $T_2^{\text{Expt.}} = 24.6 \pm 0.5 \text{ ms}$. Also shown in grey is the $\pm 5\%$ error region.

**Figure 6.**

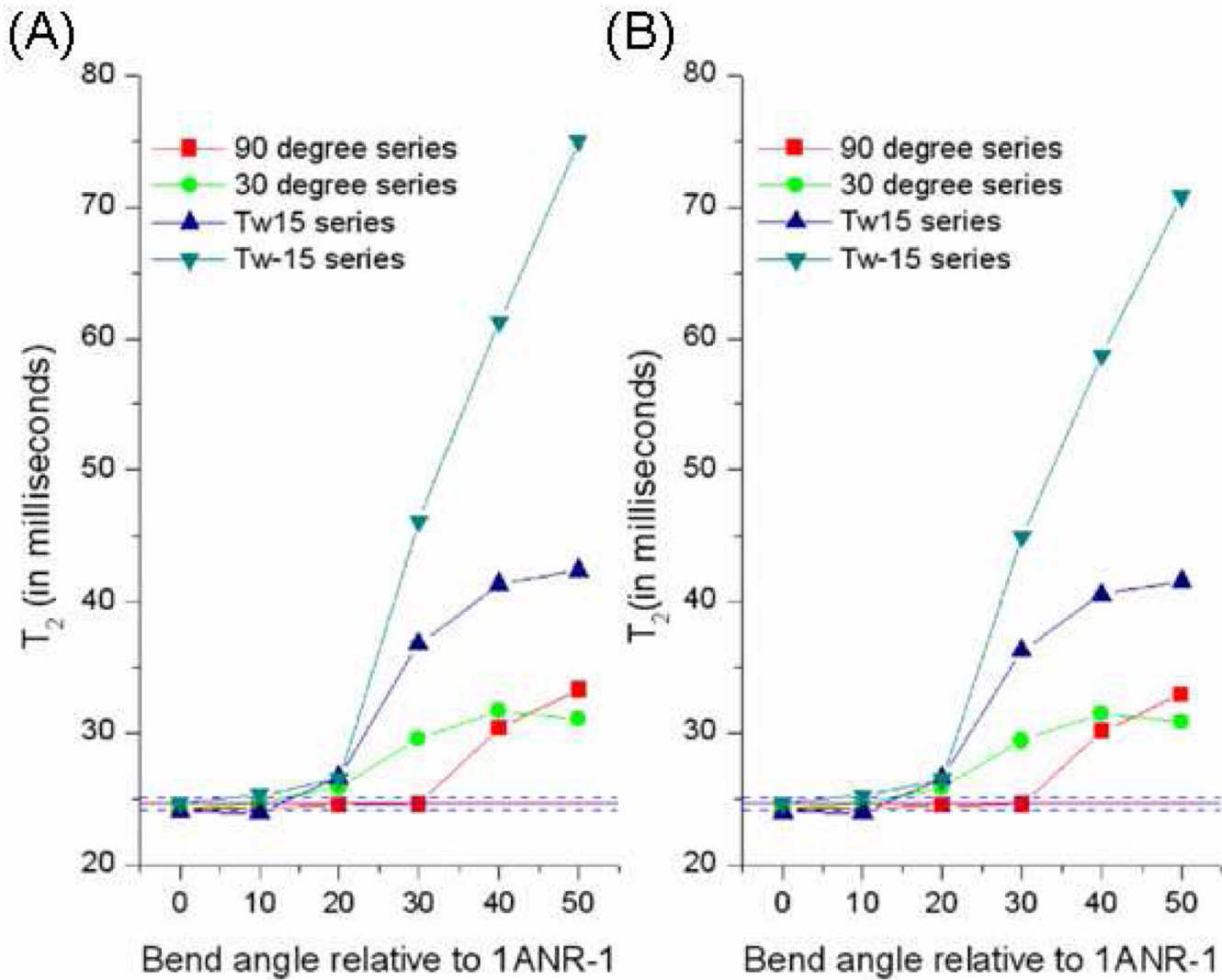
Relaxation times vs. bend angle for the “Tw15 series,” considering various exchange rates from $5 \times 10^5 \text{ s}^{-1}$ to $1 \times 10^9 \text{ s}^{-1}$: (A) T_1 times; and (B) T_2 times. Experimental values are marked by solid purple lines, and the error bars are indicated by dashed blue lines. The experimental relaxation times are: $T_1^{\text{Expt.}} = 354 \pm 3 \text{ ms}$, and $T_2^{\text{Expt.}} = 24.6 \pm 0.5 \text{ ms}$. Also shown in grey is the $\pm 5\%$ error region.

**Figure 7.**

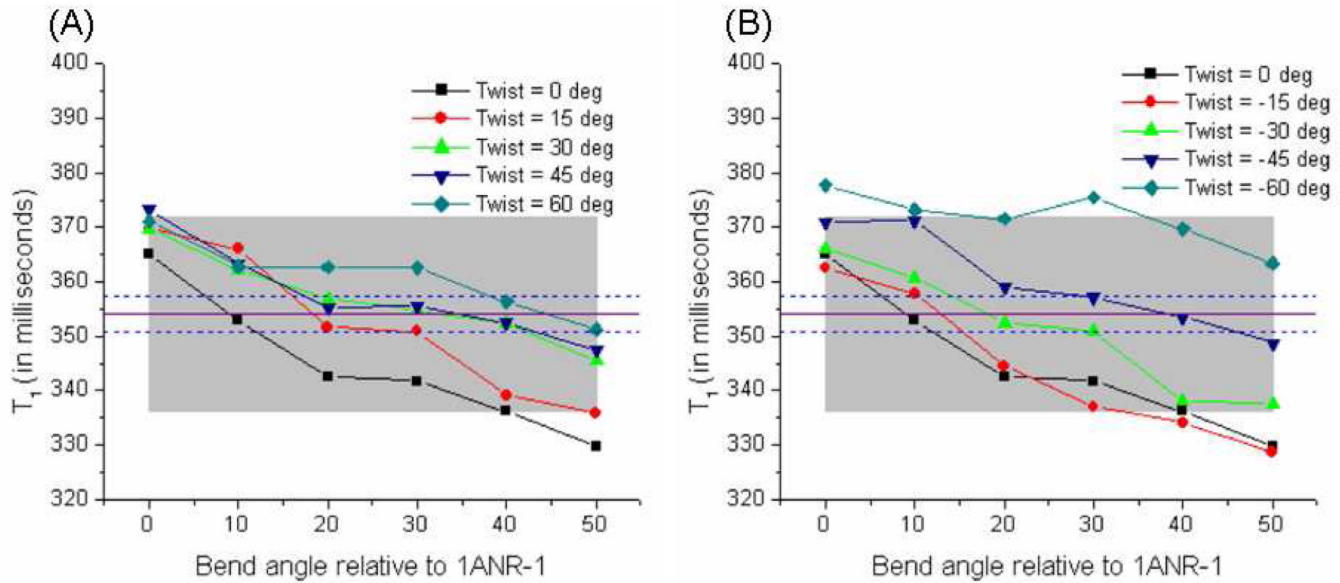
Relaxation times vs. bend angle for the “Tw-15 series,” considering various exchange rates from $5 \times 10^5 \text{ s}^{-1}$ to $1 \times 10^9 \text{ s}^{-1}$: (A) T_1 times; and (B) T_2 times. Experimental values are marked by solid purple lines, and the error bars are indicated by dashed blue lines. The experimental relaxation times are: $T_1^{\text{Expt.}} = 354 \pm 3 \text{ ms}$, and $T_2^{\text{Expt.}} = 24.6 \pm 0.5 \text{ ms}$. Also shown in grey is the $\pm 5\%$ error region.

**Figure 8.**

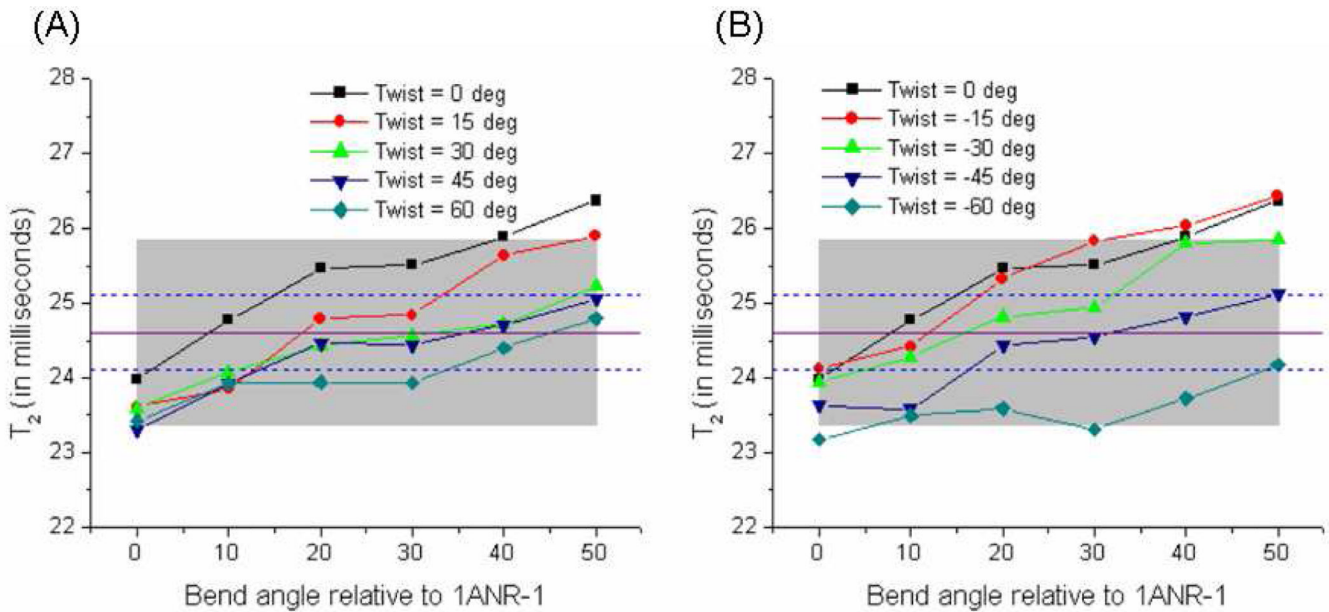
T_1 vs. bend angle for the four sets of structures for an exchange rate of: (A) $1 \times 10^{10} \text{ s}^{-1}$ and (B) $5 \times 10^9 \text{ s}^{-1}$. Experimental values are marked by solid purple lines, and the error bars are indicated by dashed blue lines. The experimental relaxation time is $T_1^{\text{Expt.}} = 354.1 \pm 3.2 \text{ ms}$. The $\pm 5\%$ error region has been left out for clarity.

**Figure 9.**

T_2 vs. bend angle for the four sets of structures for an exchange rate of: (A) $1 \times 10^{10} \text{ s}^{-1}$ and (B) $5 \times 10^9 \text{ s}^{-1}$. Experimental values are marked by solid purple lines, and the error bars are indicated by dashed blue lines. The experimental relaxation time is $T_2^{\text{Expt.}} = 24.6 \pm 0.5 \text{ ms}$. The $\pm 5\%$ error region has been left out for clarity.

**Figure 10.**

T_1 vs. bend angle, considering various degrees of twist about the upper helix, ranging from -60° to $+60^\circ$: (A) positive twist angles: 0° Twist 60° ; and (B) negative twist angles: -60° Twist 0° . Experimental values are marked by solid purple lines, and the error bars are indicated by dashed blue lines. The experimental relaxation time is $T_1^{\text{Expt.}} = 354.1 \pm 3.2$ ms. Also shown in grey is the $\pm 5\%$ error region.

**Figure 11.**

T_2 vs. bend angle, considering various degrees of twist about the upper helix, ranging from -60° to $+60^\circ$: (A) positive twist angles: 0° Twist 60° ; and (B) negative twist angles: -60° Twist 0° . Experimental values are marked by solid purple lines, and the error bars are indicated by dashed blue lines. The experimental relaxation time is $T_2^{\text{Expt.}} = 24.6 \pm 0.5$ ms. Also shown in grey is the $\pm 5\%$ error region.

Table 1

Eigenvalues and eigenvectors of the matrix $\overleftrightarrow{H}^{(2)}$ defined in Eq 10. The quantity Σ is defined as.
 $\Sigma = (D_x^2 + D_y^2 + D_z^2) - (D_x D_y + D_y D_z + D_z D_x)$.

Eigenvalue	Eigenvector elements $f_{l,k}^{(Eigenvalue)}$ (only non-zero elements are listed)
$\lambda_1 = 4D_z + 2D_{\perp} = 4D_z + D_x + D_y$	$f_{2,k=\pm 2}^{(1)} = \pm \frac{1}{\sqrt{2}}$
$\lambda_2 = 2D_z + 4D_{\perp} + \sqrt{4(D_z - D_{\perp})^2 + 3\Delta^2} = 2(D_x + D_y + D_z) + 2\sqrt{\Sigma}$	$f_{2,k=\pm 2}^{(2)} = \frac{\sqrt{6}(D_x - D_y)}{4\sqrt{2\Sigma + (D_x + D_y - 2D_z)\sqrt{\Sigma}}},$ $f_{2,k=0}^{(2)} = \frac{(D_x + D_y - 2D_z) + 2\sqrt{\Sigma}}{2\sqrt{2\Sigma + (D_x + D_y - 2D_z)\sqrt{\Sigma}}}$
$\lambda_3 = 2D_z + 4D_{\perp} - \sqrt{4(D_z - D_{\perp})^2 + 3\Delta^2} = 2(D_x + D_y + D_z) - 2\sqrt{\Sigma}$	$f_{2,k=\pm 2}^{(3)} = \frac{\sqrt{6}(D_x - D_y)}{4\sqrt{2\Sigma - (D_x + D_y - 2D_z)\sqrt{\Sigma}}},$ $f_{2,k=0}^{(3)} = \frac{(D_x + D_y - 2D_z) - 2\sqrt{\Sigma}}{2\sqrt{2\Sigma - (D_x + D_y - 2D_z)\sqrt{\Sigma}}}$
$\lambda_4 = D_z + 5D_{\perp} + \frac{3}{2}\Delta = D_z + 4D_x + D_y$	$f_{2,k=\pm 1}^{(4)} = \frac{1}{\sqrt{2}}$
$\lambda_5 = D_z + 5D_{\perp} - \frac{3}{2}\Delta = D_z + D_x + 4D_y$	$f_{2,k=\pm 1}^{(5)} = \pm \frac{1}{\sqrt{2}}$